

# Protomer alignment modulates specificity of RNA substrate recognition by Ire1

**Weihan Li<sup>1,2,7,a</sup>, Kelly Crotty<sup>1,2,a</sup>, Diego Garrido Ruiz<sup>3</sup>, Mark Voorhies<sup>4</sup>, Carlos Rivera<sup>5</sup>, Anita Sil<sup>4</sup>, R. Dyche Mullins<sup>2,6</sup>, Matthew P. Jacobson<sup>3</sup>, Jirka Peschek<sup>1,2,8,b</sup>, Peter Walter<sup>1,2,b</sup>**

<sup>1</sup> Department of Biochemistry and Biophysics, University of California San Francisco, San Francisco, CA 94143

<sup>2</sup> Howard Hughes Medical Institute

<sup>3</sup> Department of Pharmaceutical Chemistry, University of California at San Francisco, San Francisco, CA 94143

<sup>4</sup> Department of Microbiology and Immunology, University of California at San Francisco, San Francisco, CA 94143

<sup>5</sup> Department of Molecular Biophysics and Biochemistry, Yale School of Medicine, New Haven, CT 06510

<sup>6</sup> Department of Cellular and Molecular Pharmacology, University of California at San Francisco, San Francisco, CA 94143

<sup>7</sup> Current address: Department of Anatomy and Structural Biology, Albert Einstein College of Medicine, Bronx, NY 10461

<sup>8</sup> Current address: Biochemistry Center, Heidelberg University, Heidelberg, Germany

<sup>a</sup> These authors contributed equally to this work.

<sup>b</sup> Correspondence: [peter@walterlab.ucsf.edu](mailto:peter@walterlab.ucsf.edu), [jirka.peschek@bzh.uni-heidelberg.de](mailto:jirka.peschek@bzh.uni-heidelberg.de)

## Abstract

The unfolded protein response (UPR) maintains protein folding homeostasis in the endoplasmic reticulum (ER). In metazoan cells, the Ire1 branch of the UPR initiates two functional outputs—non-conventional mRNA splicing and selective mRNA decay (RIDD). By contrast, Ire1 orthologs from *Saccharomyces cerevisiae* and *Schizosaccharomyces pombe* are specialized for only splicing or RIDD, respectively. The functional specialization lies in Ire1's RNase activity, which is either stringently splice-site specific (as in *S. cerevisiae*) or promiscuous (as in *S. pombe*). Here, we developed an assay that reports on Ire1's RNase promiscuity. We found that conversion of two amino acids within the RNase domain of *S. cerevisiae* Ire1 to their *S. pombe* counterparts rendered it promiscuous. Using biochemical assays and computational modeling, we show that the mutations rewired a pair of salt bridges at Ire1 RNase domain's dimer interface, changing its protomer alignment. Thus, Ire1 protomer alignment affects its substrates specificity.

## Introduction

In eukaryotes, about one third of all proteins are folded in the endoplasmic reticulum (ER). The protein folding homeostasis of the ER is monitored and tightly regulated by a collective of signaling pathways, known as the unfolded protein response (UPR) (Hetz, Zhang, & Kaufman, 2020; Walter & Ron, 2011). The most evolutionarily conserved branch of the UPR is initiated by Ire1, an ER-transmembrane kinase/endoribonuclease (RNase). In response to accumulated unfolded proteins in the ER, Ire1 forms oligomers (Aragon et al., 2009; Korennykh et al., 2009; H. Li, Korennykh, Behrman, & Walter, 2010) and carries out two functional outputs. First, Ire1 initiates non-conventional splicing of *HAC1* (in *S. cerevisiae*) or *XBP1* (in metazoans) mRNA (Cox, Shamu, & Walter, 1993; Mori, Ma, Gething, & Sambrook, 1993; Sidrauski & Walter, 1997; Yoshida, Matsui, Yamamoto, Okada, & Mori, 2001). After cleavage by Ire1 and removal of the intron, the severed exons are ligated by tRNA ligase (Jurkin et al., 2014; Kosmaczewski et al., 2014; Lu, Liang, & Wang, 2014; Peschek, Acosta-Alvear, Mendez, & Walter, 2015; Peschek & Walter, 2019; Sidrauski, Cox, & Walter, 1996). The spliced mRNAs are translated into Hac1 and Xbp1 proteins, both of which are transcription factors that induce the UPR gene expression program in the nucleus (Calfon et al., 2002; Travers et al., 2000; Van Dalfsen et al., 2018; Yoshida et al., 2001). Second, Ire1 selectively cleaves a set of mRNAs that encode ER-targeted proteins. The cleaved mRNAs are subsequently degraded by the cellular RNA decay machinery (Guydosh, Kimmig, Walter, & Green, 2017). As a result, this process, known as regulated Ire1-dependent mRNA decay (RIDD), restores homeostasis of the ER by reducing the protein folding burden (Bae, Moore, Mella, Hayashi, & Hollien, 2019; Hollien et al., 2009; Hollien & Weissman, 2006; Kimmig et al., 2012; Moore & Hollien, 2015).

While metazoan Ire1 performs both functions, the Ire1 orthologs in *Saccharomyces cerevisiae* and *Schizosaccharomyces pombe* are functionally specialized: *S. cerevisiae* Ire1 initiates splicing of *HAC1* mRNA as its singular target in the cell (Niwa, Patil, DeRisi, & Walter, 2005), and *S. pombe* Ire1 exclusively performs RIDD (Guydosh et al., 2017; Kimmig et al., 2012). Our previous study reported that the functional specialization of Ire1 is achieved through diverged RNase specificities (W. Li et al., 2018). *S. cerevisiae* Ire1 has a stringent RNase, restricting it to *HAC1* mRNA. In contrast, *S. pombe* Ire1 has a promiscuous (i.e. broadly specific) RNase, enabling cleavage of a wide range of mRNA RIDD targets. Which structural determinants on Ire1 influence RNase specificity remained unknown. Here, we addressed this question by mutagenesis-guided biochemical analyses and structural modeling.

# Results

## Promiscuous RNase activity of *S. pombe* Ire1 is toxic to bacterial cells

We recently purified and characterized recombinant *S. cerevisiae* (*Sc*) and *S. pombe* (*Sp*) Ire1 kinase/RNase (KR) domains (W. Li et al., 2018). During the protein expression process, we noticed that the presence of plasmids bearing the genes encoding *Sc* and *Sp* Ire1-KR under the control of the T7 promoter differently affected growth of the *E. coli* host cells. Growth curves revealed that *E. coli* cells bearing a plasmid containing the *Sp* *IRE1-KR* barely grew within the monitored 5 h time window, even in the absence of the isopropyl  $\beta$ -D-thiogalactopyranoside (IPTG) inducer (Figure 1A, blue filled triangles). By contrast, *E. coli* cells bearing plasmids containing *Sc* *IRE1-KR* grew normally with a growth rate comparable to that of a control strain bearing an empty plasmid. Because the T7 promoter is known to exhibit background expression even in the absence of IPTG (Rosano & Ceccarelli, 2014), we reasoned that the observed gene toxicity of *Sp* *IRE1-KR* might result from the enzyme's promiscuous RNase activity, which may degrade endogenous *E. coli* RNAs required for viability. By contrast, *Sc* Ire1-KR might be tolerated, because of its exquisite substrate specificity for *Sc* *HAC1* mRNA splice junctions (Niwa et al., 2005). To test this notion, we used the Ire1 RNase inhibitor 4 $\mu$ 8C (Cross et al., 2012). As expected, 4 $\mu$ 8C inhibited cleavage of a 21 base-pair stem-loop substrate derived from the 3' splice junction of *XBP1* mRNA for both *Sp* and *Sc* Ire1-KR (Figure 1B and C), as well as RIDD activity in *Sp* cells (Figure 1-figure supplement 1). Importantly, when added to the cultures of cells bearing plasmids encoding *Sp* Ire1-KR, 4 $\mu$ 8C restored normal growth (Figure 1A). In further agreement with the notion that *Sp* RNase activity was the culprit of reduced *E. coli* growth, an RNase-dead mutant of *Sp* Ire1-KR harboring the H1018A mutation (Kimmig et al., 2012) was not toxic (Figure 1A). These results suggest that *E. coli* growth was inhibited by the endonuclease activity, rather than by indirect effects, such as protein misfolding or aggregation. Moreover, we established that bacterial growth can be exploited to assess substrate specificity of Ire1's RNase.

## Ire1's RNase domain confers promiscuous RNase activity

We reasoned that this assay might allow us to glean insights into Ire1's substrate specificity. Using structure-guided sequence comparison of Ire1 RNase domains, we picked a total of seventeen residues whose common features include that they are i) part of an oligomerization interface or located within 18 Å from the helix-loop element (HLE), which contains a positively charged loop (N1036 to K1042 on *Sc* Ire1) that engages the RNA



substrates (Korennykh et al., 2009; Korennykh et al., 2011; Lee et al., 2008), and ii) divergent amino acids between *Sc* and *Sp* but conserved within the *Schizosaccharomyces* genus. Among the seventeen amino acids, seven are located near the HLE, five are located at the RNase-RNase interface within the back-to-back dimer (previously defined as interface IF1<sup>C</sup> (Korennykh et al., 2009)), and five are located at the RNase-RNase interface in the active Ire1 oligomer (previously defined as interface IF2<sup>C</sup> (Korennykh et al., 2009)) (Figure 2A & B, Figure 2 - table supplement 1).

To examine possible effects of these residues on RNase specificity, we cloned and purified an *Sc* Ire1-KR mutant with all 17 residues replaced by their *S. pombe* counterparts (*Sc* Ire1-KR-mut17). We tested its RNase activity using four previously characterized stem-loop RNA substrates derived from the *Sc HAC1* mRNA 3' splice site that is exclusively cleaved by *Sc* Ire1, as well as the Ire1 cleavage sites of the *Sp BIP1*, *PLB1* and *SPAC4G9.15* mRNAs that are exclusively cleaved by *Sp* Ire1 (W. Li et al., 2018). We chose the three *Sp* RNA substrates because their Ire1 cleavage sites vary in predicted loop sizes (9-, 7- and 3-membered loops, respectively). Cleavage activity towards stem-loop RNAs with variable loop sizes is one of the characteristic features of Ire1 promiscuity (W. Li et al., 2018). In agreement with previous results, wildtype (WT) *Sc* Ire1-KR cleaved the *HAC1* mRNA 3' splice site but none of the *Sp* stem-loop RNA substrates. Remarkably, *Sc* Ire1-KR-mut17 efficiently and specifically cleaved all four stem-loop RNA substrates (Figure 2 C-F) with comparable kinetics (Figure 2G & Figure 2-figure supplement 1). These results show that introducing the 17 mutations made *Sc* Ire1 more “pombe-like” regarding its acceptance of variable-loop RIDD substrates. When tested in the *E. coli* growth assay, the expression of Ire1-KR-mut17 proved toxic and 4μ8C alleviated the toxicity (Figure 2H), confirming the notion that toxicity results from the enzyme’s broadened substrate range.

### **Residues at Ire1’s dimer interface confer RNase promiscuity**

The above results demonstrate that bacterial growth can be a useful readout for Ire1’s RNase promiscuity. Hence, we used this assay to identify the residue(s) that were causal in conferring the broadened substrate specificity of *Sc* Ire1-KR-mut17. To this end, we created single revertants, each with one of the seventeen mutations was converted back to the original amino acid in *Sc*. We expected that when we revert a mutation that contributes to the enzyme’s broadened substrate specificity, the revertant would be stringent and less toxic to *E. coli* cells. We found that 3 revertants (K992, H1044, and Y1059) showed markedly reduced toxicity, whereas the other 14 revertants remained toxic (Figure 3A). Next, we cloned and purified a

mutant protein, *Sc* Ire1-KR(K992D,H1044D,Y1059R), in which we combined the three identified mutations. *Sc* Ire1-KR(K992D,H1044D,Y1059R) cleaved both *Sp* stem-loop and *Sc* *HAC1* 3' splice-site substrates efficiently (Figure 3 B-E) and with similar rates (Figure 3F & Figure 3-figure supplement 1). These results narrowed the list of candidate amino acid changes that confer RNase promiscuity down to three.

Based on the locations of these three residues, we divided them into two groups. *Sc* Ire1 K992 and Y1059 (corresponding to D950 and R1016 of *Sp* Ire1) are located at Ire1's back-to-back dimer interface, while *Sc* Ire1 H1044 (corresponding to *Sp* Ire1 D1001) is located two amino acids C-terminal of the HLE. We cloned and purified two Ire1 mutants, *Sc* Ire1-KR(K992D,Y1059R) and *Sc* Ire1-KR(H1044D). Recombinantly expressed and purified *Sc* Ire1-KR(K992D,Y1059R) cleaved both *Sc* and *Sp* stem-loop RNA substrates with efficiencies comparable to those of *Sc* Ire1-KR(K992D,H1044D,Y1059R) (Figure 3B-F). By contrast, *Sc* Ire1-KR(H1044D) cleaved the cognate *Sc* RNA substrate but none of the *Sp* RNA substrates (Figure 3 B-F), suggesting that the two *cerevisiae*-to-*pombe* mutations at Ire1's RNase-RNase dimer interface confer Ire1 RNase promiscuity. By contrast, H1044D appears a false positive, likely isolated because the bacterial assay cannot distinguish stringent RNase from inactive RNase as neither is toxic to the bacterial cells.

### ***S. cerevisiae* Ire1-KR(K992D,Y1059R) recognizes RNA substrates with reduced stringency**

*Sc* Ire1 displays a strong preference for RNA substrates that contain a consensus sequence within a stem-loop structure (Gonzalez, Sidrauski, Dorfler, & Walter, 1999; Hooks & Griffiths-Jones, 2011; W. Li et al., 2018; Oikawa, Tokuda, Hosoda, & Iwawaki, 2010). We next characterized the RNA motif recognized by *Sc* Ire1-KR(K992D,Y1059R) and compared it to those recognized by WT *Sc* and *Sp* Ire1-KR. To this end, we examined Ire1 cleavage efficiencies on a series of *HAC1*- and *BIP1*-derived mutant stem-loop RNAs, in which each loop residue was individually changed into the three other possible ribonucleotides (Figure 4A & B). Using the *HAC1*-derived mutant substrates, we showed that WT *Sc* Ire1-KR showed specificity for the sequence motif CNG|(C/A)NGN, in close agreement with previous findings (Gonzalez et al., 1999). By comparison, *Sc* Ire1-KR(K992D,Y1059R) recognized a less-stringent sequence motif, CNG|NNGN, in particular tolerating base substitutions in the +1 position (Figure 4A).

To assess the effects of RNA loop size variation on Ire1 cleavage efficiency, we engineered mutations at positions -4 to break the base-pairing at the tip of the stem and enlarge the loop from 7 to 9 nucleotides. The 9-membered stem loops were not cleaved by WT *Sc* Ire1-

KR, in line with previous study (Gonzalez et al., 1999). By contrast, the same RNAs were cleaved by *Sc* Ire1-KR(K992D,Y1059R) (Figure 4A). The results suggest that the two interface mutations in *Sc* Ire1-KR(K992D,Y1059R) render the enzyme more tolerant to both RNA sequence and loop size variations.

The Ire1 cleavage site in *Sp* *BIP1* mRNA contains a 9-nucleotide loop with a UG|C cleavage site shifted by one nucleotide (Figure 4B). We confirmed that a stem-loop RNA substrate containing this site was efficiently cleaved by *Sp* Ire1-KR but not by *Sc* Ire1-KR, in agreement with our previous reports (Guydosh et al., 2017; Kimmig et al., 2012; W. Li et al., 2018). By contrast, *Sc* Ire1-KR(K992D,Y1059R) cleaved the motif efficiently with the additional tolerance of any nucleotide at position -2, thus reducing the required sequence motif to only G and C nucleotides flanking the cleavage site (Figure 4B). G|C is likewise present at the *PLB1* and *SPAC4G9.15* mRNA cleavage sites embedded in 7- and 3-membered loops, respectively, which also proved to be substrates of *Sc* Ire1-KR(K992D,Y1059R) (Figure 3B-E). In further support of the notion that *Sp* Ire1-KR and *Sc* Ire1-KR(K992D,Y1059R) are tolerant to loop size variation, two of our stem-loop RNA substrates harboring mutations,  $U_{-5} \rightarrow A$  and  $U_{+4} \rightarrow A$ , respectively, which are predicted to contract the 9-membered loop to a 7-membered one, were efficiently cleaved by both enzymes (Figure 4B). Together, these data affirm the notion that *Sp* Ire1-KR and *Sc* Ire1-KR(K992D,Y1059R) are promiscuous enzymes that recognize short RNA sequence motifs and can accept a range of loop sizes.

### **Salt-bridge rewiring at Ire1's dimer interface confers promiscuous RNase activity**

To understand how the interface mutations confer promiscuous RNase activity, we explored structural differences between *Sp* Ire1, *Sc* Ire1 and *Sc* Ire1-KR(K992D,Y1059R) using molecular modeling. Active *Sc* Ire1 oligomers are composed of multiple Ire1 back-to-back dimers that stack in a helical arrangement (Korennykh et al., 2009). K992 and Y1059 are located at the RNase-RNase interface of the back-to-back assembly of Ire1 protomers in PDB 3FBV (protomer A and B in Figure 5A). To build a structural model of *Sc* Ire1-KR(K992D,Y1059R), we introduced K992D and Y1059R onto the *Sc* Ire1 dimer structure and performed energy minimization to optimize distances and resolve steric clashes. We followed this calculation with molecular dynamics (MD) simulations, comparing *Sc* Ire1-KR(K992D,Y1059R) and WT *Sc* Ire1-KR. Analysis was performed from 10 ns to 20 ns, and the simulation structures reached equilibrium within 10 ns (Figure 5-figure supplement 1). The convergent structure model of *Sc* Ire1-KR(K992D,Y1059R) predicts a structural rearrangement at Ire1's dimer interface. Specifically, whereas in the WT *Sc* Ire1-KR dimer residues E988 and

K992 of both protomers form a symmetric pair of salt bridges across the dimer interface (Figure 5B), these salt bridges are absent in the dimer of *Sc* Ire1-KR(K992D,Y1059R) due to the charge reversal introduced by the K992D mutation. More interestingly, the model predicts the formation of a new pair of salt bridges in *Sc* Ire1-KR(K992D,Y1059R), connecting the two newly introduced amino acids D992 and R1059 across the protomer/protomer interface (Figure 5C). The MD simulation predicts these new bonds as stable features (Figure 5-figure supplement 2). Thus, molecular modeling suggests a structural rearrangement, resulting from the two interface mutations in *Sc* Ire1, which, we propose, allows *Sc* Ire1 to assume the promiscuous “*pombe*-like” state (Figure 5D).

The predicted new salt bridges in *Sc* Ire1-KR(K992D,Y1059R) are mediated by guanidinium-carboxylate bidentate interactions, which are among the strongest non-covalent interactions in proteins and are considerably stronger than the ammonium-carboxylate interaction seen in the salt bridges in WT *Sc* Ire1-KR (Masunov & Lazaridis, 2003). Given that the interaction at the dimer interface is predicted to be stronger in mutant *Sc* Ire1-KR(K992D,Y1059R) than in WT *Sc* Ire1-KR, the mutant enzyme should be more prone to form dimers/oligomers than WT *Sc* Ire1-KR. Indeed, we confirmed this notion using protein crosslinking *in vitro*, followed by SDS-PAGE, showing that WT *Sc* Ire1-KR was mostly monomeric, while *Sc* Ire1-KR(K992D,Y1059R) formed mostly dimers and tetramers (Figure 5E, compare lanes 2 and 3 with lanes 6 and 7). We further verified this result using sedimentation equilibrium analytical ultracentrifugation (Figure 5-figure supplement 3). For *Sc* Ire1-KR(K992D,Y1059R), we calculated a dissociation constant ( $K_D$ ) of 0.98  $\mu$ M, which is about 60-fold smaller than that of WT *Sc* Ire1-KR ( $K_D$  = 57  $\mu$ M). Based on these results, we consider it likely that the estimated gain in free energy of the predicted new salt bridges results in higher affinity within the back-to-back dimer, thus increasing the propensity of Ire1 to oligomerize.

Next, we experimentally tested the predicted salt bridges using mutagenesis. To this end, we first engineered *Sc* Ire1-KR(K992D,Y1059A), introducing an alanine at position 1059. This Ire1 mutant can neither form *S. cerevisiae*-like nor *S. pombe*-like salt bridges (Figure 5D). Thus, as expected, *Sc* Ire1-KR(K992D,Y1059A) did not form dimers (Figure 5E, lanes 8 and 9) and displayed ~100-fold reduced cleavage efficiency on *HAC1*-derived and an additional 100-fold (i.e., overall ~10,000-fold) reduced cleavage rate on *BIP1*-derived RNA substrates (Figure 5-figure supplement 4). Thus, surprisingly, breaking the *pombe*-like salt bridge arrangement restored *Sc* Ire1’s ability to discriminate between substrate RNAs by ~100-fold (Figure 5F).

Breaking the predicted salt bridges on *Sc* Ire1-KR(K992D,Y1059R) by mutating aspartate 992 to alanine also abolished Ire1’s RNase activity (*Sc* Ire1-KR(K992A,Y1059R);

Figure 5-figure supplement 4), in this case reducing activity towards both *HAC1*- and *BIP1*-derived substrate RNAs beyond our detection limit (>10,000-fold). Thus, we were not able to assess substrate specificity for this mutant.

Finally, we generated a charge-reversal mutant of *Sc* Ire1-KR(K992D,Y1059R) by changing aspartate 992 to arginine and arginine 1059 to aspartate (*Sc* Ire1-KR(K992R,Y1059D)). We expected these two mutations to restore the salt bridges predicted for *Sc* Ire1-KR(K992D,Y1059R) but with reversed polarity. We found that, while the overall cleavage rate remained 100-fold suppressed for both RNA substrates, *Sc* Ire1-KR(K992R,Y1059D) regained activity towards the *BIP1*-derived substrate (Figure 5F, Figure 5-figure supplement 4) and formed dimers (Figure 5E, lanes 10 and 11). Together, these experiments validate the predicted salt bridges on *Sc* Ire1-KR(K992D,Y1059R) and further underscore the notion that salt bridge rewiring to a pombe-like arrangement confers promiscuity to Ire1's RNase activity.

The importance of both types of salt bridges is further highlighted by a sequence comparison of 230 Ire1 orthologs from yeast to human (see Figure 5G for a partial list of the Ire1 orthologs; a complete list is included in Figure 5-figure supplement 5 and its figure source file). We compared residues at three positions corresponding to the *Sc* Ire1 E988, K992 and Y1059. We found that 175 out of 230 of the Ire1 orthologs, including human Ire1 $\alpha$  and Ire1 $\beta$ , have the *S. pombe*-like pattern, characterized by significant amino acid variation at position 988, a negatively charged amino acid (aspartate or glutamate) at position 992, and a positively charged amino acid (lysine or arginine) at position 1059. The apparent co-evolution of position 992 and 1059 further supports the existence of an inter-molecular salt bridge. Thirty-three out of 230 of the Ire1 orthologs have the *S. cerevisiae*-like pattern—with a negatively charged amino acid (aspartate or glutamate) at position 988, a positively charged amino acid (lysine or arginine) at position 992 and, in most cases, a tyrosine at position 1059. Co-evolution of position 988 and 992 supports their interaction at the dimer interface.

# **Interface mutations change the protomer alignment in Ire1 dimer**

To gain an appreciation of how the interface mutations affect Ire1's active RNase site in the dimer, we compared the structure of WT *Sc* Ire1-KR dimer with the predicted structure of *Sc* Ire1-KR(K992D,Y1059R) dimer after aligning the two KR dimers by one protomer (Figure 6A and B for front and bottom-up view, respectively). Interestingly, we observed a rocking motion between the RNase domains of the protomers (Figure 6B). Specifically, the salt bridge between D992 and R1059' in *Sc* Ire1-KR(K992D,Y1059R) reduced the distance between the two

juxtaposed  $\alpha$ -helices from which their sidechains protrude ( $\alpha$ 1-Helix: aa 983-998;  $\alpha$ 4-Helix: aa 1048-1064, as named in (Lee et al., 2008)) (Figure 6C), while, concomitantly, the loss of the salt bridges between E988 and K992 present in WT Sc Ire1-KR allows an increase in the distance between  $\alpha$ 1-Helices from which both of these amino acid side chains protrude (Figure 6D). We used two metrics to quantify this change. First, we measured the distance between the centers of mass of the two  $\alpha$ 1-Helices throughout the 20 ns simulation trajectories, which was increased by about 3 Å in Sc Ire1-KR(K992D,Y1059R) compared to WT Sc Ire1-KR. This measurement reflects the changes in protomer alignment caused by the salt bridge rewiring. Second, we measured the distance between the  $\alpha$  carbons of R1039 involved in RNA substrate binding and H1061' involved in phosphodiester bond hydrolysis (Korennykh et al., 2011), which was decreased by about 5 Å in Sc Ire1-KR(K992D,Y1059R) compared to WT Sc Ire1-KR (Figure 6E, F). Therefore, the mutations that increase Ire1's RNase promiscuity are predicted to change both the RNase-RNase interface and the relative alignment of important elements in the catalytic site of the Ire1 dimer.



# Discussion

From both an evolutionary and mechanistic angle, it has long been a puzzle how two modalities of Ire1 function arose and are structurally implemented. At one extreme lies Ire1 from *S. cerevisiae*, which is highly specific, precisely cleaving but a single mRNA in the cell (*HAC1* mRNA) at its two splice junctions to excise the intron and initiate mRNA splicing. At the other extreme lies Ire1 from *S. pombe*, which is highly promiscuous cleaving numerous mRNAs at recognition sites that share but a three-nucleotide consensus in a variably sized loop. Cleavage in this case initiates mRNA breakdown by RIDD. We previously showed by domain swapping experiments that Ire1's cytosolic kinase/RNase domains determine whether Ire1 works in the specific *S. cerevisiae*-like or relatively non-specific *S. pombe*-like modality. Using a growth assay based on heterologous expression of Ire1 kinase/RNase domains in bacteria that reports on Ire1's RNase promiscuity, we found that the *S. cerevisiae* Ire1's RNase specificity becomes promiscuous when only two amino acids, K992 and Y1059, are replaced by aspartate and arginine respectively, which are the corresponding amino acids in *S. pombe* Ire1. While these replacements rendered Sc Ire1 more promiscuous, they did not entirely switch Sc Ire1's substrate RNA profile to that of Sp Ire1: Sc Ire1-KR(K992D,Y1059R) retained activity towards *HAC1* mRNA-derived stem-loops, which is inert to cleavage by Sp Ire1 (W. Li et al., 2018). The K992D and Y1059R mutations therefore rendered Sc Ire1 even more promiscuous than Sp Ire1.

MD simulations and biochemical assays revealed that the identified residues cause rewiring of two symmetry-related inter-molecular salt-bridges at Ire1's RNase-RNase interface within the back-to-back dimer. Sequence comparison of Ire1 orthologs showed that this rewiring is conserved and, where known, correlates with reported functional outputs (Cheon et al., 2011; Hollien et al., 2009; Hollien & Weissman, 2006; Miyazaki & Kohno, 2014; Miyazaki, Nakayama, Nagayoshi, Kakeya, & Kohno, 2013). By this criterion, the vast majority of species is predicted to have RIDD-enabled Ire1s as indicated by their *S. pombe*-like salt bridge pattern. Even though human Ire1 $\alpha$  and Ire1 $\beta$  have different RNase specificity (Imagawa, Hosoda, Sasaka, Tsuru, & Kohno, 2008), both have a *S. pombe*-like interface pattern. This characteristic is consistent with both human isoforms being able to perform RIDD (Hollien et al., 2009; Iwawaki et al., 2001). Of note, the ability of Sc Ire1-KR(K992D,Y1059R) to conduct both *HAC1*-specific and promiscuous cleavage resembles that of human Ire1 $\alpha$  in its fully phosphorylated, oligomeric state, while the more restricted activity of Sc Ire1 resembles that of dimeric human Ire1 $\alpha$  (Le Thomas et al., in preparation).

Surprisingly, our work identified the RNase-RNase interface, rather than regions involved in substrate binding or catalysis, as a determinant for Ire1's RNase specificity. We show evidence that conserved salt bridges determine the relative protomer alignment. In the composite RNase active site of the back-to-back dimer, the relative distance of residues that contribute to cleavage from both protomers is changed (Korennykh et al., 2011). The small molecule, quercetin, which stabilizes *S. cerevisiae* Ire1's dimers/oligomers and increase its RNase activity (Wiseman et al., 2010), binds to the same site where the two mutations identified in this study are located. However, quercetin binding does not change Ire1 protomer alignment and hence is not expected to alter Ire1's RNase specificity (Wiseman et al., 2010). Nevertheless, modulation of the RNase selectivity by targeting the quercetin pocket is conceivable. In human Ire1, crystal structures showed that the two RNase domains in the dimer are further apart in the inactive state than in the active state (Joshi et al., 2015), and our data similarly indicate that breaking the salt bridges in Sc Ire1-KR(K992D,Y1059R) by either changing the aspartate or the arginine to alanine leads to profound reduction of activity. Related work demonstrates that the more promiscuous RIDD modality of human Ire1 $\alpha$  requires phosphorylation-driven oligomerization, which can be prevented by an oligomer-disrupting mutation at the RNase-RNase interface within the back-to-back dimers (Le Thomas et al., in preparation). Thus together, the data presented here demonstrate that Ire1 RNase domain's dimer interface is a dynamic site through which both activity and substrate specificity can be regulated.



## **Acknowledgment**

We thank Avi Ashkenazi, Adrien Le Thomas, Wallace Marshall, Jonathan Weissman, Marc Shuman and members of the Walter lab for their insightful discussions. This work was supported by UCSF-Zaffaroni Fellowship (WL), the Human Frontier Science Program (JP), NIH/NIAID 2R37 AI066224 (AS), NIH R01 GM032384 (PW), 1R35 GM118119-01 (DW), Howard Hughes Medical Institute EXROP (CR). JP is an Emmy Noether fellow of the Deutsche Forschungsgemeinschaft. PW and DM are Investigators of the Howard Hughes Medical Institute.

## **Competing Financial Interests**

The authors declare no competing financial interests.

## Materials and Methods

### Recombinant protein expression and purification

The cytoplasmic portion of *Sc* or *Sp* Ire1 containing its kinase and RNase domains (Ire1-KR) was expressed and purified from BL21-CodonPlus (DE3)-RIPL *Escherichia coli*. We used an expression vector which fuses a PreScission Protease cleavage site between the Ire1-KR and glutathione S-transferase (GST) domains of the recombinant polypeptide and was regulated by a T7 promoter. The expression cassette was transformed into *E. coli* cells. The WT *Sc* Ire1-KR was expressed as described previously (Korennnykh et al., 2009). For *E. coli* cells transformed with plasmids containing the *Sp* Ire1-KR or *Sc* Ire1-KR mutant, all colonies on the transformation plate were collected 16 h after transformation and mixed with 50 mL of LB medium. After 3 h incubation at 37°C, the sample was diluted to 12 L of LB medium and further incubated at 37°C until optical density reached 1. The incubation temperature was reduced to 25°C and protein expression was induced by adding IPTG to a final concentration of 0.5 mM. After 4 h of growth at 25°C, the cells were pelleted by centrifugation.

Cells were resuspended in GST binding buffer (50 mM Tris-HCl pH 7.5, 500 mM NaCl, 2 mM Mg(OAc)<sub>2</sub>, 2 mM DTT, 10% glycerol) and homogenized using high-pressure homogenizer (EmulsiFlex). The cell lysate was applied to a GST-affinity column and eluted with GST elution buffer (50 mM Tris-HCl pH 7.5, 200 mM NaCl, 2 mM Mg(OAc)<sub>2</sub>, 2 mM DTT, 10% glycerol, 10 mM reduced glutathione). The column elution was treated with GST-tagged HRV 3C protease (PreScission Protease, GE Health) to cleave off the GST tag. At the same time, the sample was dialyzed to remove glutathione in the elution buffer. After 12 h dialysis, the sample was further purified through negative chromatography by passing through a GST-affinity column (GSTrap FF Columns, GE Healthcare Life Sciences) to remove free GST, residual GST-fused Ire1 KR, and GST-tagged protease, and a Q FF anion exchange column (GE Healthcare Life Sciences) to remove contaminating nucleic acids. The flow-through containing untagged Ire1 KR was further purified by applying it to a Superdex 200 16/60 gel filtration column (GE healthcare) and then concentrated to 20-40 µM in storage buffer (50 mM Tris-HCl pH 7.5, 500 mM NaCl, 2 mM Mg(OAc)<sub>2</sub>, 2 mM TCEP, 10% glycerol) and flash-frozen in liquid nitrogen. The final purity, as well as purity at intermediate steps, was assessed by SDS-PAGE using Coomassie blue staining.

### In vitro RNA cleavage assay

Short RNA oligos derived from the Ire1 cleavage sites on *Sp BIP1* mRNA, *SPAC4G9.15* mRNA, *PLB1* mRNA, and the *Sc HAC1* mRNA 3' splice site were purchased from Dharmacon, Inc. The sequence of stem-loop RNA substrates ordered were the following: *Sp BIP1* cleavage site: 5'CGCGAGAUAAACUGGUGCUUUGUUAUCUCGCG, *Sp SPAC4G9.15* cleavage site: 5'CCACCACCGAGUAUGCUACUCGGUGGUGG, *Sp PLB1* cleavage site: 5'ACGGCCUUUGUUGCAAAAGGGUGCGU (25bp), and *Sc HAC1* 3' splice site: 5'GCGCGGACUGUCCGAAGCGCAGUCCGCGC. RNA oligos were gel extracted, acetone precipitated, and resuspended in RNase-free water. The oligos were 5'-end radiolabeled with gamma-[<sup>32</sup>P]-ATP (Perkin Elmer) using T4 polynucleotide kinase (NEB) and cleaned using ssDNA/RNA Clean and Concentrator kit (Zymo Research D7010).

To fold the RNA, we heated the RNA oligos to 90°C for 3 min and slowly cooled them down at a rate of 1°C per minute until the temperature reached 10°C. In the Ire1 cleavage assays, the reaction samples contained 12.5 μM of Ire1-KR. The cleavage reaction was performed as described previously (W. Li et al., 2018) by incubating at 30°C in reaction buffer (50 mM Tris/HCl pH 7.5, 200 mM NaCl, 2 mM Mg(OAc)<sub>2</sub>, 2 mM TCEP, 10% glycerol). For reactions in Figure 1B & C, 200 μM of 4μ8C (Sigma-Aldrich) was added. At each time point, an aliquot was transferred to 1.2x STOP buffer (10 M urea, 0.1% SDS, 1 mM EDTA, trace amounts bromophenol blue). RNAs were separated using denaturing 15% Novex™ TBE-Urea Gels (ThermoFisher) and transferred to Amersham Hybond-N+ membranes. Radioactive RNA membranes were imaged with a Phosphorimager (Typhoon FLA 9500, GE Health). The band intensities were quantified using ImageJ. The cleaved portion was calculated as the cleaved band intensity divided by the sum of the cleaved band and uncleaved band intensities. The  $k_{obs}$  values were obtained by fitting the data to first-order 'one-phase' decay equations using Prism (GraphPad).

# **In vitro RNA cleavage assay of *HAC1*- and *BIP1*-derived RNA mutants**

*In vitro* transcription of the mutant RNA stem-loops derived from the *HAC1* 3' splice site and *BIP1* cleavage site were carried out as follows. Single-stranded DNA oligonucleotides were used as templates to which the 18mer 5'TAATACGACTCACTATAG "T7 promoter oligonucleotide" was annealed to create a double-stranded T7 RNA polymerase promoter. The templates contain the indicated single point mutations from Figure 4 on the following parent oligonucleotides: *HAC1*-27 (encoding wild-type *HAC1* 3' stem-loop RNA with T7 promoter): 5'GCGCGGACTGCGTTCGGACAGTCCGCCTATAGTGAGTCGTATTA, and *BIP1*-32 (encoding

wild-type *BIP1* stem-loop RNA with T7 promoter):

5'CGCGAGATAACAAAGCACCAAGTTATCTCGCGCTATAGTGAGTCGTATTA.

A solution containing 5 nM T7 promoter oligonucleotide and 0.75 nM template oligonucleotide was heated to 100°C for 3 min and immediately placed on ice. 20 µL transcription reactions containing 5 µL of the template solution, 1 mM each of ATP, CTP, GTP, and UTP, 1x reaction buffer, and 2 µL T7 RNA Polymerase mix (HiScribe T7 High Yield RNA Synthesis Kit, NEB) were incubated at 37°C for 3 h. RNA oligos were gel extracted in 300 µL RNase-free water. These RNA substrates are not radio labeled. The RNAs are folded, cleaved by Ire1-KR and separated by TBE-Urea gels in the same way as the radio labeled RNAs. The TBE-Urea gels were stained with SYBR Gold (ThermoFisher) and imaged on the Typhoon with excitation at 488 nm. The emission was collected using a band pass filter at 550 nm. Image analysis is the same as radio labeled RNAs.

## Bacterial growth assays

Expression vectors containing the *Sc* Ire1-KR, *Sp* Ire1-KR, or a mutant form of these proteins regulated by a T7 promoter were transformed into BL21-CodonPlus (DE3)-RIPL *E. coli* cells. Freshly transformed *E. coli* cells were cultured overnight (~20 h) and then diluted to an OD<sub>600</sub> of 0.02. The cultures were incubated at 37°C and their OD<sub>600</sub> was obtained every 15 min by the Tecan Spark Multimode Microplate Reader (Life Sciences) (60 cycle kinetic loop, continuous shaking, double orbital 2.5 mm, 108 rpm) for 5 h. For cultures containing the Ire1 RNase inhibitor 4µ8C, 1 µM of 4µ8C (Sigma-Aldrich) was added into both the overnight culture and the diluted culture. It is important to use freshly transformed (transformed within 72 h) *E. coli* cells as the toxicity of *Sp* Ire1-KR and mutants of *Sc* Ire1-KR accumulates over time.

## Crosslinking gel

Each Ire1 construct was buffer-exchanged three times with Zeba spin desalting columns (ThermoFisher Scientific 89882) into a buffer containing 50 mM HEPES, 200 mM NaCl, 2 mM Mg(OAc)<sub>2</sub>, 2 mM TCEP, and 10% Glycerol. 8 µL crosslinking reactions containing 12.5 µM Ire1, 2 mM ADP, and 1 mM BS3 crosslinker (ThermoFisher Scientific 21580) were carried out on ice for two hours and quenched by adding concentrated Tris-HCl to a final concentration of 60 mM. The entire reaction was separated on an SDS-PAGE gel, stained with SYPRO Ruby (ThermoFisher Scientific S21900) or coomassie blue overnight and scanned with the Typhoon FLA 9500 or Gel Documentation system (Bio-Rad) respectively.

## Analytical Ultracentrifugation

Experiments were performed in a Beckman Coulter Optima XL-A analytical ultracentrifuge equipped with UV-visible absorbance detection system using a 4-hole An-60 Ti analytical rotor. Multi-speed sedimentation equilibrium experiments were carried out at 20°C and 7,000, 10,000, and 14,000 rpm until equilibrium was reached for 110 µL samples of concentrations of 10 µM, 5 µM, and 2.5 µM protein. Samples were dialyzed overnight into analysis buffer (50 mM Tris/HCl, pH 7.5, 200 mM NaCl, 2 mM Mg(OAc)<sub>2</sub>, 2 mM TCEP) to remove glycerol. Analysis buffer without protein was used as reference. Measurements were made at 280 nm in the absorbance optics mode. Raw data were trimmed using WinReEdit (Jeff W. Lary, University of Connecticut) and globally fitted to a self-association equilibrium model using WinNonlin using all concentrations and speeds for each protein sample.

## Molecular dynamics simulation

All simulations were performed using the Amber suite (Case et al., 2014). Initial structure and topology files were prepared in LEaP (Sastry, Adzhigirey, Day, Annabhimoju, & Sherman, 2013) using the Amber ff12SB force field, the general Amber force field (gaff) and the phosaa10 parameters for phosphorylated amino acids. The structural model included an inhibitor bound to the kinase domain that was kept in place for the simulations. Inhibitor parametrization was performed using AnterChamber (Wang, Wang, Kollman, & Case, 2006; Wang, Wolf, Caldwell, Kollman, & Case, 2004). We solvated the system with TIP3P water molecules in a periodic cubic box such that the closest distance between the periodic boundary and the closest atom in the protein was 10 Å. We added counterions to neutralize the box.

We minimized the energy of the system, first using harmonic restraints on the protein backbone (10 kcal mol<sup>-1</sup> Å<sup>-2</sup>) then in an unrestrained minimization, for 500 steps of steepest descent and 500 steps of conjugate gradient, each at constant volume with a non-bonded cutoff distance of 9 Å.

We performed a three-step equilibration: 1. heating the system to 300 K at constant volume with harmonic restraints on the protein backbone (10 kcal mol<sup>-1</sup> Å<sup>-2</sup>) at constant volume using the SHAKE algorithm (Ciccotti & Ryckaert, 1986) constraining bonds involving hydrogens and the Andersen thermostat for 20 ps; 2. constant pressure of 1 bar with lower restraints on the protein backbone (1 kcal mol<sup>-1</sup> Å<sup>-2</sup>) for 20 ps with consistent parameters; 3. the restraints on the protein backbone were released and the system was equilibrated at constant pressure for 1 ns.

We seeded the production runs with random new velocities at constant pressure of 1 bar and a non-bonded cutoff distance of 9 Å and ran the molecular dynamics simulations for 20 ns

with a 2 fs time step. Coordinates and energy were saved every picosecond (500 steps). We assessed the convergence of the simulations by examining backbone root-mean-square deviation (RMSD) plots with particular focus on the RNase domain.

Visual inspection of molecular models was performed using ChimeraX (Goddard et al., 2018), a virtual reality implementation of the traditional molecular visualization program. Molecular graphics and analyses performed with UCSF Chimera (Pettersen et al., 2004), developed by the Resource for Biocomputing, Visualization, and Informatics at the University of California, San Francisco, with support from NIH P41-GM103311.

### **Ire1 deep alignment**

Ire1 orthologs were identified by searching the Pfam Ribonuc\_2-5A hidden Markov model (HMM) with HMMSEARCH from HMMER 3.1b2 (Eddy, 2011) against all proteins from RefSeq fungal genomes downloaded from GenBank 1/17/2017 plus six plant genomes (*C. elegans*, *D. melanogaster*, *D. rerio*, *M. musculus*, *M. mulatta*, and *H. sapiens*) and six animal genomes (*A. thaliana*, *C. reinhardtii*, *P. patens*, *O. sativa*, *S. lycopersicum*, and *P. glauca*) downloaded from GenBank 7/19/2019. This gave predominantly hits to Ire1 orthologs. Outlier hits to RNaseL and difficult to place microsporidian RNases were removed. A guide multiple alignment was generated by PROBCONS 1.12 alignment (Do, Mahabhashyam, Brudno, & Batzoglou, 2005) of the Ire1 hits from plants and animals plus 14 fungal species (*H. capsulatum*, *A. nidulans*, *N. crassa*, *F. graminearum*, *Y. lipolytica*, *S. cerevisiae*, *C. albicans*, *K. lactis*, *S. pombe*, *P. carinii*, *C. neoformans*, *U. maydis*, *P. graminis*, and *M. verticillata*). HMMBUILD was used to generate an HMM from the conserved regions of the PROBCONS alignment, spanning the kinase and RNase domains. HMMALIGN was then used to realign the full set of Ire1 hits to the new HMM. A maximum likelihood phylogeny was estimated from the aligned positions with FASTTREE 2.1.8 (Price, Dehal, & Arkin, 2010). The resulting tree was rendered with an in-house PYTHON script.

**Figure 1. The promiscuous RNase activity of *S. pombe* Ire1 causes toxicity to bacterial cells.** (A) Growth curves of bacterial cells expressing various Ire1 kinase-RNase (KR) domains. Optical densities at 600 nm (OD<sub>600</sub>) were measured every 15 min for 5 h. Bacterial cells expressing *S. cerevisiae* (Sc) or *S. pombe* (Sp) Ire1-KR were incubated at 37°C. In the indicated samples, 1 µM of the Ire1's RNase inhibitor 4µ8C was added to the culture. The *Sp* Ire1-KR(H1018A) has a catalytically inactive RNase. (B, C) In vitro RNA cleavage assays with or without 200 µM of 4µ8C. 5' radio-labeled stem-loop RNA substrates, which are derived from the *XBP1* mRNA 3' splice site, were incubated with 12.5 µM of *Sp* (B) or *Sc* (C) Ire1-KR at 30°C for the indicated time.



**Figure 2. *S. cerevisiae* Ire1-KR-mut17 has a promiscuous RNase activity. (A)**

Sequence alignment of the RNase domains of Ire1 orthologs from *Saccharomyces cerevisiae*, *Schizosaccharomyces pombe*, *Schizosaccharomyces octosporus*, *Schizosaccharomyces cryophilus*. A total of 17 residues (green) were selected as the candidate residues that may regulate Ire1's RNase promiscuity. These candidate residues are located at back-to-back dimer interface (marked with \*), oligomer interface (marked with +) or near the helix loop element (marked with ^). Sequence of the helix loop element (HLE) is underlined. (B) The location of the 17 candidate residues (green) on the back-to-back dimer structure of the Ire1 cytosolic domain (PDB: 3FBV) with kinase domain in yellow and RNase domain in purple. The dimer interface, oligomer interface and HLE regions are indicated in dashed boxes. (C-F) In vitro RNA cleavage assays with 12.5  $\mu$ M of wildtype (WT) Sc Ire1-KR or Sc Ire1-KR-mut17. The stem-loop RNA substrates are derived from the Sc *HAC1* mRNA 3' splice site (C), *Sp BIP1* (D), *PLB1* (E) and *SPAC4G9.15* (F) mRNA cleavage sites. Experimental conditions are the same as in Figure 1B&C. Predicted RNA secondary structures are illustrated. Ire1 cleavage sites are marked with red dashed lines. (G) Comparison of the  $k_{obs}$  of WT Sc Ire1-KR, Sc Ire1-KR-mut17 and *Sp* Ire1-KR. The  $k_{obs}$  of WT Sc Ire1-KR and Sc Ire1-KR-mut17 were calculated from experiments in (C-F). The  $k_{obs}$  of *Sp* Ire1-KR was measured under the same condition from our previous study (W. Li et al., 2018). "BD" indicates cleavage activity below detection limit. Experiments were performed in duplicates. (H) Bacterial growth assay for WT Sc Ire1-KR, Sc Ire1-KR-mut17 and *Sp* Ire1-KR. Experimental conditions are the same as in Figure 1A. In the indicated samples, 1  $\mu$ M of 4 $\mu$ 8C was added.



**Figure 3. Two residues at Ire1's RNase-RNase dimer interface regulate Ire1's RNase promiscuity.** (A) Bacterial growth assay for *Sc* Ire1-KR revertants. Conditions are the same as in Figure 1A. OD<sub>600</sub> at 5-hour time-point was measured. Experiments were performed in duplicates. Dashed line marks the threshold used to separate toxic and non-toxic Ire1 constructs. (B-E) In vitro cleavage assays of *Sc* Ire1-KR(K992D,H1044D,Y1059R), *Sc* Ire1-KR(K992D,Y1059R) and *Sc* Ire1-KR(H1044D) on *Sc HAC1* mRNA 3' splice site (B), *Sp BIP1* (C), *PLB1* (D) and *SPAC4G9.15* (E) mRNA cleavage sites. Experimental conditions are the same as in Figure 1C. (F) Comparison of the  $k_{obs}$  that are calculated from results in (B-E). "BD" indicates cleavage activity below detection limit. Experiments were performed in duplicates.

**Figure 4. *S. cerevisiae* Ire1-KR(K992D,Y1059R) has a promiscuous RNase activity.**

(A-B) A series of twenty-four (A) and twenty-seven (B) stem-loop RNA substrates, which are derived from the *S. cerevisiae* *HAC1* mRNA 3' splice site (A) or the *S. pombe* *BIP1* mRNA cleavage site (B), are in vitro transcribed. Each of the substrate carries a single-point mutation, which is located on the loop or at the end position of the stem. The sequence of the various point mutations is indicated next to each residue (above the line). Listed below these sequences are the cleavage efficiencies, at which each mutant RNA substrate was cleaved by Sc Ire1-KR (first row below the line in panel A), *Sp* Ire1-KR (first row below the line in panel B) or Sc Ire1-KR(K992D,Y1059R) (second rows below the lines in panels A and B).  $k_{obs}$  of mutant stem-loop RNAs is normalized to  $k_{obs}$  of WT *HAC1* (A) or *BIP1* (B) stem-loop RNAs that are cleaved by the corresponding Ire1. (-) is no cleavage; (-/+) is 1-10%; (+) is 10-60%; (++) is 60-120%; (+++) is > 120%. Ire1 cleavage sites are marked with red dashed lines. Yellow squares (in A), blue squares (in B) and grey circles (in A and B) mark the positions, at which specific residues are required to achieve efficient cleavages by Sc Ire1-KR, *Sp* Ire1-KR and Sc Ire1-KR(K992D,Y1059R), respectively. Experimental conditions are the same as in Figure 1C.

**Figure 5. Structural re-arrangement at Ire1 dimer interface regulates the RNase promiscuity.** (A) Back-to-back dimer structure of WT *Sc* Ire1 cytosolic domain (PDB: 3FBV) with kinase domain in yellow and RNase domain in purple. K992 and Y1059 are colored in green while E988 is colored in blue. Side chain labels on protomer B are marked with '. (B) Close-up view focusing on the interface region of WT *Sc* Ire1 dimer. Dashed lines indicate salt bridges. (C) Close-up view focusing on the interface region of the predicted dimer structure of *Sc* Ire1-KR(K992D,Y1059R), which was generated by a 20-ns molecular dynamics (MD) simulation from an initial structural model that was built from the WT *Sc* Ire1 dimer (PDB: 3FBV). The final frame of the simulation was illustrated. D992 and R1059 are colored in green while E988 is colored in blue. Dashed lines indicate salt bridges. (D) Illustration of the residues at *Sc* Ire1 position 988, 992 and 1059 (or *Sp* Ire1 position 946, 950 and 1016). Dashed lines indicate salt bridges. (E) Crosslinking gel for various Ire1-KR constructs. Indicated Ire1-KR (12.5  $\mu$ M) constructs were incubated with or without 1 mM of crosslinker bissulfosuccinimidyl suberate for 2 h on ice before being separated on an SDS-PAGE gel and stained by coomassie blue. (F) Ire1's ability to distinguish *Sc* *HAC1*- and *Sp* *BIP1*-derived RNA substrates is measured by the ratio of their corresponding  $k_{obs}$ . (G) Evolutionary comparison of Ire1 orthologs from various species. The analysis focuses on three residues, which correspond to position 988, 992 and 1059 on *Sc* Ire1. The *S. cerevisiae*-like pattern (yellow) has an E/D at 988, K/R at 992 and Y at 1059. The *S. pombe*-like pattern (blue) has a varying amino acid (aa) at 988, D/E at 992 and K/R at 1059.

**Figure 6. Interface mutations change the protomer alignment in Ire1 dimer. (A)**

Structure alignment of WT *Sc* Ire1-KR and *Sc* Ire1-KR(K992D,Y1059R). 20-ns MD simulations were performed on both WT *Sc* Ire1-KR and *Sc* Ire1-KR(K992D,Y1059R). The last simulation frame was used for structure alignment. The protomer A of the two dimers were aligned with minimal root mean square deviation. *Sc* Ire1-KR(K992D,Y1059R) is in grey. WT *Sc* Ire1-KR has its kinase domain in yellow and RNase domain in purple. The  $\alpha$ 1-Helix at position 983-998,  $\alpha$ 4-Helix at position 1048-1064, H1061, and R1039 are in red, pink, yellow and cyan, respectively. (B, C) Bottom-up view of the aligned RNase domains (B), and the  $\alpha$ 1- and  $\alpha$ 4-Helix (C). Side chains of D992 and R1059 are shown. Dashed lines are salt bridges. (D) Side view of  $\alpha$ 1-Helices. Color coding are the same as in (A). Side chain labels on protomer B are marked with '. (E) Measuring Ire1 protomer alignment in the MD simulation. Y-axis is the distance between the centers of mass of the two  $\alpha$ 1-Helices. X-axis is the distance between the  $\alpha$ -carbons of R1039 on protomer A and H1061 on protomer B. Each dot represents a time point in the MD simulation. Measurements of WT *Sc* Ire1-KR are in yellow while measurements of *Sc* Ire1-KR(K992D,Y1059R) are in grey. (F) Cartoon illustration showing the protomer alignment of WT *Sc* Ire1-KR and *Sc* Ire1-KR(K992D,Y1059R). Their RNase domains were zoomed in with double-arrow lines showing the distances being measured in (E).

**Figure 1-figure supplement 1. Ire1's RNase inhibitor 4μ8C inhibits *S. pombe* Ire1's activity in vivo.** 200 ul of WT *S. pombe* cell culture at OD<sub>600</sub> 0.5 was evenly spread onto YE5S plate, which does or doesn't contain 0.05 μg/ml of tunicamycin. Circular Whatman paper (diameter ~1 cm) was placed onto the YE5S plates. 5 ul of DMSO or 4μ8C (at concentration of 1 mM) was spotted onto the Whatman papers. Plates were incubated at 30°C for 3 days.

**Figure 2-figure supplement 1. Quantification of in vitro cleavage assays.** Results

from the in vitro cleavage assays in Figure 2C-F were quantified using ImageJ. Cleaved portion was calculated as: cleaved RNA / (cleaved RNA + uncleaved RNA). When the cleaved portion is  $\geq 0.1$  at time point 30 min, data was fitted to a first-order exponential function. When the cleaved portion is  $< 0.1$  at time point 30 min, data was fitted to a linear function. Experiments were performed in duplicates.

**Figure 2-table supplement 1. A list of the 17 candidate residues on *S. cerevisiae* and *S. pombe* Ire1.** The oligomer interface is referred as the interface IF2<sup>C</sup> and the back-to-back dimer interface is referred as the interface IF1<sup>C</sup> in (Korennykh et al., 2009).

**Figure 3-figure supplement 1. Quantification of in vitro cleavage assays.** Results from the in vitro cleavage assays in Figure 3B-E were quantified and analyzed using the same methods as in Figure 2-figure supplement 1.



629           **Figure 3-table supplement 1. The detailed sequence information of *S. cerevisiae***  
630 **Ire1-KR constructs used in this study.** “Y” indicates the mutation is present in the  
631 corresponding Ire1 construct. “N” indicates the mutation is absent in the corresponding Ire1  
632 construct.  
633

**Figure 5-figure supplement 1. The root-mean-square deviation (RMSD) of atomic positions of Ire1 RNase domain during the simulation.** Result of WT Sc Ire1-KR is in yellow and Sc Ire1-KR(K992D,Y1059R) is in grey.

**Figure 5-figure supplement 2. Time fraction of the MD simulation during which the indicated salt bridges are present.** A 20-ns MD simulation was performed on the dimer structure of WT Sc Ire1 KR or Sc Ire1-KR(K992D,Y1059R). At a given time point during the simulation, if the distance between the two indicated residues is smaller than 2.5 Å, the two residues are considered to be connected by a salt bridge. The bar graph shows the accumulative time fraction during which each indicated salt bridge is present. Side chain on protomer B are marked with ‘.

**Figure 5-figure supplement 3. Sedimentation equilibrium analytical**

**ultracentrifugation (SE-AUC) analysis of Sc Ire1-KR and Sc Ire1-KR(K992D,Y1059R).** Each protein was examined under nine conditions: at three protein concentrations (2.5, 5 and 10  $\mu$ M) and three centrifugal speeds (7,000, 10,000, and 14,000 rpm). All nine datasets for each protein were fitted to an equilibrium model. (A) WT Sc Ire1-KR was mostly monomeric at the concentrations tested and had a monomer-dimer equilibrium constant of 57.3  $\mu$ M. (B) Sc Ire1-KR(K992D,Y1059R) showed a higher propensity to form dimers/tetramers than WT Sc Ire1 KR, with a monomer-dimer equilibrium constant of 0.981  $\mu$ M. (C) Plot of the natural logarithm of the absorbance at 280 nm versus the square of the spin radius for the 10  $\mu$ M Sc Ire1-KR and Sc Ire1-KR(K992D,Y1059R) samples at 7,000 rpm.

**Figure 5-figure supplement 4. RNA cleavage efficiencies of *Sc* Ire1-KR mutants bearing mutations at back-to-back dimer interface.**  $k_{\text{obs}}$  of the indicated *Sc* Ire1-KR constructs cleaving stem-loop RNA substrates derived from *Sc HAC1* mRNA 3' splice site or *Sp BIP1* mRNA cleavage site. "BD" indicates cleavage activity below detection limit.

# **Figure 5-figure supplement 5. Evolutionary comparison of Ire1 orthologs.**

We generated a deep alignment of 230 Ire1 orthologs from fungi (211), representative plants (9) and animals (10). We compared residues at three positions, which correspond to the *S. cerevisiae* Ire1 E988, K992 and Y1059. Among the 230 orthologs being analyzed, 175 of them have the *S. pombe*-like pattern (blue)—with a varying amino acid at position 988, a negatively charged amino acid (aspartate or glutamate) at position 992 and a positively charged amino acid (lysine or arginine) at position 1059. 33 of the Ire1 orthologs have the *S. cerevisiae*-like pattern—with a negatively charged amino acid (aspartate or glutamate) at position 988, a positively charged amino acid (lysine or arginine) at position 992 and mostly tyrosine at position 1059. Tyrosine at position 1059 may orchestrate the positioning of lysine/arginine side chain at position 992 (Lee et al., 2008). The *S. cerevisiae*-like pattern is restricted to the Saccharomycotina. In 6 Ire1 orthologs, the *S. cerevisiae*- or *S. pombe*-like inter-molecular salt bridge are replaced with a putative hydrogen bond (marked with x). Ire1 orthologs from higher plants exhibit a pattern distinct from *S. cerevisiae* and *S. pombe*. One interesting case (Table insert A) is with the Ire1 from *Yarrowia lipolytica*, whose location on the evolutionary tree is at the boundary between *S. cerevisiae*-like and *S. pombe*-like species. *Yarrowia lipolytica* Ire1 is in a transitioning state from the *S. cerevisiae*-like into the *S. pombe*-like Ire1—its amino acids at position 988 (aspartate) and 1059 (tyrosine) remain *S. cerevisiae*-like whereas its amino acid at position 992 (glutamate) changed from *S. cerevisiae*-like (positively charged) into *S. pombe*-like (negatively charged). The case of *Yarrowia lipolytica* Ire1 suggests that salt-bridge rewiring occurs during the evolutionary process. Another interesting case (Table insert B) is with the Ire1 from *Capronia epimyces*. While its neighboring species have *S. pombe*-like pattern, *Capronia epimyces* Ire1 undergoes a unique evolution with arginine, aspartate and methionine at positions 988, 992 and 1059, making it a charge reversal (at positions 988 and 992) of *S. cerevisiae*-like Ire1. The detailed sequences are listed in the figure source file.

**Table 1. Plasmids used in this study.** In all of the plasmids, a GST and an HRV 3C protease site are N-terminally fused to Ire1-KR.

# References

- Aragon, T., van Anken, E., Pincus, D., Serafimova, I. M., Korennykh, A. V., Rubio, C. A., & Walter, P. (2009). Messenger RNA targeting to endoplasmic reticulum stress signalling sites. *Nature*, 457(7230), 736-740. doi:10.1038/nature07641
- Bae, D., Moore, K. A., Mella, J. M., Hayashi, S. Y., & Hollien, J. (2019). Degradation of Blos1 mRNA by IRE1 repositions lysosomes and protects cells from stress. *J Cell Biol*, 218(4), 1118-1127. doi:10.1083/jcb.201809027
- Calton, M., Zeng, H., Urano, F., Till, J. H., Hubbard, S. R., Harding, H. P., . . . Ron, D. (2002). IRE1 couples endoplasmic reticulum load to secretory capacity by processing the XBP-1 mRNA. *Nature*, 415(6867), 92-96. doi:10.1038/415092a
- Case, D., Babin, V., Berryman, J., Betz, R., Cai, Q., Cerutti, D., . . . Gohlke, H. (2014). Amber14 Reference manual. 2014. *Table of Contents graphic*, 1(2), 3.
- Cheon, S. A., Jung, K. W., Chen, Y. L., Heitman, J., Bahn, Y. S., & Kang, H. A. (2011). Unique evolution of the UPR pathway with a novel bZIP transcription factor, Hxl1, for controlling pathogenicity of *Cryptococcus neoformans*. *PLoS Pathog*, 7(8), e1002177. doi:10.1371/journal.ppat.1002177
- Ciccotti, G., & Ryckaert, J.-P. (1986). Molecular dynamics simulation of rigid molecules. *Computer Physics Reports*, 4(6), 346-392.
- Cox, J. S., Shamu, C. E., & Walter, P. (1993). Transcriptional induction of genes encoding endoplasmic reticulum resident proteins requires a transmembrane protein kinase. *Cell*, 73(6), 1197-1206. doi:10.1016/0092-8674(93)90648-a
- Cross, B. C., Bond, P. J., Sadowski, P. G., Jha, B. K., Zak, J., Goodman, J. M., . . . Harding, H. P. (2012). The molecular basis for selective inhibition of unconventional mRNA splicing by an IRE1-binding small molecule. *Proc Natl Acad Sci U S A*, 109(15), E869-878. doi:10.1073/pnas.1115623109
- Do, C. B., Mahabhashyam, M. S., Brudno, M., & Batzoglou, S. (2005). ProbCons: Probabilistic consistency-based multiple sequence alignment. *Genome Res*, 15(2), 330-340. doi:10.1101/gr.2821705
- Eddy, S. R. (2011). Accelerated Profile HMM Searches. *PLoS Comput Biol*, 7(10), e1002195. doi:10.1371/journal.pcbi.1002195
- Goddard, T. D., Huang, C. C., Meng, E. C., Pettersen, E. F., Couch, G. S., Morris, J. H., & Ferrin, T. E. (2018). UCSF ChimeraX: Meeting modern challenges in visualization and analysis. *Protein Sci*, 27(1), 14-25. doi:10.1002/pro.3235
- Gonzalez, T. N., Sidrauski, C., Dorfler, S., & Walter, P. (1999). Mechanism of non-spliceosomal mRNA splicing in the unfolded protein response pathway. *EMBO J*, 18(11), 3119-3132. doi:10.1093/emboj/18.11.3119
- Guydosh, N. R., Kimmig, P., Walter, P., & Green, R. (2017). Regulated Ire1-dependent mRNA decay requires no-go mRNA degradation to maintain endoplasmic reticulum homeostasis in *S. pombe*. *eLife*, 6. doi:10.7554/eLife.29216
- Hetz, C., Zhang, K., & Kaufman, R. J. (2020). Mechanisms, regulation and functions of the unfolded protein response. *Nat Rev Mol Cell Biol*, 21(8), 421-438. doi:10.1038/s41580-020-0250-z



Hollien, J., Lin, J. H., Li, H., Stevens, N., Walter, P., & Weissman, J. S. (2009). Regulated Ire1-dependent decay of messenger RNAs in mammalian cells. *J Cell Biol*, 186(3), 323-331. doi:10.1083/jcb.200903014

Hollien, J., & Weissman, J. S. (2006). Decay of endoplasmic reticulum-localized mRNAs during the unfolded protein response. *Science*, 313(5783), 104-107. doi:10.1126/science.1129631

Hooks, K. B., & Griffiths-Jones, S. (2011). Conserved RNA structures in the non-canonical Hac1/Xbp1 intron. *RNA Biol*, 8(4), 552-556. doi:10.4161/rna.8.4.15396

Imagawa, Y., Hosoda, A., Sasaka, S., Tsuru, A., & Kohno, K. (2008). RNase domains determine the functional difference between IRE1alpha and IRE1beta. *FEBS Lett*, 582(5), 656-660. doi:10.1016/j.febslet.2008.01.038

Iwawaki, T., Hosoda, A., Okuda, T., Kamigori, Y., Nomura-Furuwatari, C., Kimata, Y., . . . Kohno, K. (2001). Translational control by the ER transmembrane kinase/ribonuclease IRE1 under ER stress. *Nat Cell Biol*, 3(2), 158-164. doi:10.1038/35055065

Joshi, A., Newbatt, Y., McAndrew, P. C., Stubbs, M., Burke, R., Richards, M. W., . . . Bayliss, R. (2015). Molecular mechanisms of human IRE1 activation through dimerization and ligand binding. *Oncotarget*, 6(15), 13019-13035. doi:10.18632/oncotarget.3864

Jurkin, J., Henkel, T., Nielsen, A. F., Minnich, M., Popow, J., Kaufmann, T., . . . Martinez, J. (2014). The mammalian tRNA ligase complex mediates splicing of XBP1 mRNA and controls antibody secretion in plasma cells. *EMBO J*, 33(24), 2922-2936. doi:10.15252/embj.201490332

Kimmig, P., Diaz, M., Zheng, J., Williams, C. C., Lang, A., Aragon, T., . . . Walter, P. (2012). The unfolded protein response in fission yeast modulates stability of select mRNAs to maintain protein homeostasis. *eLife*, 1, e00048. doi:10.7554/eLife.00048

Korennykh, A. V., Egea, P. F., Korostelev, A. A., Finer-Moore, J., Zhang, C., Shokat, K. M., . . . Walter, P. (2009). The unfolded protein response signals through high-order assembly of Ire1. *Nature*, 457(7230), 687-693. doi:10.1038/nature07661

Korennykh, A. V., Korostelev, A. A., Egea, P. F., Finer-Moore, J., Stroud, R. M., Zhang, C., . . . Walter, P. (2011). Structural and functional basis for RNA cleavage by Ire1. *BMC Biol*, 9, 47. doi:10.1186/1741-7007-9-47

Kosmaczewski, S. G., Edwards, T. J., Han, S. M., Eckwahl, M. J., Meyer, B. I., Peach, S., . . . Hammarlund, M. (2014). The RtcB RNA ligase is an essential component of the metazoan unfolded protein response. *EMBO Rep*, 15(12), 1278-1285. doi:10.15252/embr.201439531

Lee, K. P., Dey, M., Neculai, D., Cao, C., Dever, T. E., & Sicheri, F. (2008). Structure of the dual enzyme Ire1 reveals the basis for catalysis and regulation in nonconventional RNA splicing. *Cell*, 132(1), 89-100. doi:10.1016/j.cell.2007.10.057

Li, H., Korennykh, A. V., Behrman, S. L., & Walter, P. (2010). Mammalian endoplasmic reticulum stress sensor IRE1 signals by dynamic clustering. *Proc Natl Acad Sci U S A*, 107(37), 16113-16118. doi:10.1073/pnas.1010580107

Li, W., Okreglak, V., Peschek, J., Kimmig, P., Zubradt, M., Weissman, J. S., & Walter, P. (2018). Engineering ER-stress dependent non-conventional mRNA splicing. *eLife*, 7. doi:10.7554/eLife.35388

Lu, Y., Liang, F. X., & Wang, X. (2014). A synthetic biology approach identifies the mammalian UPR RNA ligase RtcB. *Mol Cell*, 55(5), 758-770. doi:10.1016/j.molcel.2014.06.032

Masunov, A., & Lazaridis, T. (2003). Potentials of mean force between ionizable amino acid side chains in water. *J Am Chem Soc*, 125(7), 1722-1730. doi:10.1021/ja025521w

Miyazaki, T., & Kohno, S. (2014). ER stress response mechanisms in the pathogenic yeast *Candida glabrata* and their roles in virulence. *Virulence*, 5(2), 365-370. doi:10.4161/viru.27373

Miyazaki, T., Nakayama, H., Nagayoshi, Y., Kakeya, H., & Kohno, S. (2013). Dissection of Ire1 functions reveals stress response mechanisms uniquely evolved in *Candida glabrata*. *PLoS Pathog*, 9(1), e1003160. doi:10.1371/journal.ppat.1003160

Moore, K., & Hollien, J. (2015). Ire1-mediated decay in mammalian cells relies on mRNA sequence, structure, and translational status. *Mol Biol Cell*, 26(16), 2873-2884. doi:10.1091/mbc.E15-02-0074

Mori, K., Ma, W., Gething, M. J., & Sambrook, J. (1993). A transmembrane protein with a cdc2+/CDC28-related kinase activity is required for signaling from the ER to the nucleus. *Cell*, 74(4), 743-756. doi:10.1016/0092-8674(93)90521-q

Niwa, M., Patil, C. K., DeRisi, J., & Walter, P. (2005). Genome-scale approaches for discovering novel nonconventional splicing substrates of the Ire1 nuclease. *Genome Biol*, 6(1), R3. doi:10.1186/gb-2004-6-1-r3

Oikawa, D., Tokuda, M., Hosoda, A., & Iwawaki, T. (2010). Identification of a consensus element recognized and cleaved by IRE1 alpha. *Nucleic Acids Res*, 38(18), 6265-6273. doi:10.1093/nar/gkq452

Peschek, J., Acosta-Alvear, D., Mendez, A. S., & Walter, P. (2015). A conformational RNA zipper promotes intron ejection during non-conventional XBP1 mRNA splicing. *EMBO Rep*, 16(12), 1688-1698. doi:10.15252/embr.201540955

Peschek, J., & Walter, P. (2019). tRNA ligase structure reveals kinetic competition between non-conventional mRNA splicing and mRNA decay. *eLife*, 8. doi:10.7554/eLife.44199

Pettersen, E. F., Goddard, T. D., Huang, C. C., Couch, G. S., Greenblatt, D. M., Meng, E. C., & Ferrin, T. E. (2004). UCSF Chimera--a visualization system for exploratory research and analysis. *J Comput Chem*, 25(13), 1605-1612. doi:10.1002/jcc.20084

Price, M. N., Dehal, P. S., & Arkin, A. P. (2010). FastTree 2--approximately maximum-likelihood trees for large alignments. *PLoS One*, 5(3), e9490. doi:10.1371/journal.pone.0009490

Rosano, G. L., & Ceccarelli, E. A. (2014). Recombinant protein expression in *Escherichia coli*: advances and challenges. *Front Microbiol*, 5, 172. doi:10.3389/fmicb.2014.00172

Sastry, G. M., Adzhigirey, M., Day, T., Annabhimoju, R., & Sherman, W. (2013). Protein and ligand preparation: parameters, protocols, and influence on virtual screening enrichments. *J Comput Aided Mol Des*, 27(3), 221-234. doi:10.1007/s10822-013-9644-8

Sidrauski, C., Cox, J. S., & Walter, P. (1996). tRNA ligase is required for regulated mRNA splicing in the unfolded protein response. *Cell*, 87(3), 405-413. doi:10.1016/s0092-8674(00)81361-6

Sidrauski, C., & Walter, P. (1997). The transmembrane kinase Ire1p is a site-specific endonuclease that initiates mRNA splicing in the unfolded protein response. *Cell*, 90(6), 1031-1039. doi:10.1016/s0092-8674(00)80369-4

Travers, K. J., Patil, C. K., Wodicka, L., Lockhart, D. J., Weissman, J. S., & Walter, P. (2000). Functional and genomic analyses reveal an essential coordination between the unfolded protein response and ER-associated degradation. *Cell*, 101(3), 249-258. doi:10.1016/s0092-8674(00)80835-1

Van Dalen, K. M., Hodapp, S., Keskin, A., Otto, G. M., Berdan, C. A., Higdon, A., . . . Brar, G. A. (2018). Global Proteome Remodeling during ER Stress Involves Hac1-Driven Expression of Long Undecoded Transcript Isoforms. *Dev Cell*, 46(2), 219-235 e218. doi:10.1016/j.devcel.2018.06.016

Walter, P., & Ron, D. (2011). The unfolded protein response: from stress pathway to homeostatic regulation. *Science*, 334(6059), 1081-1086. doi:10.1126/science.1209038

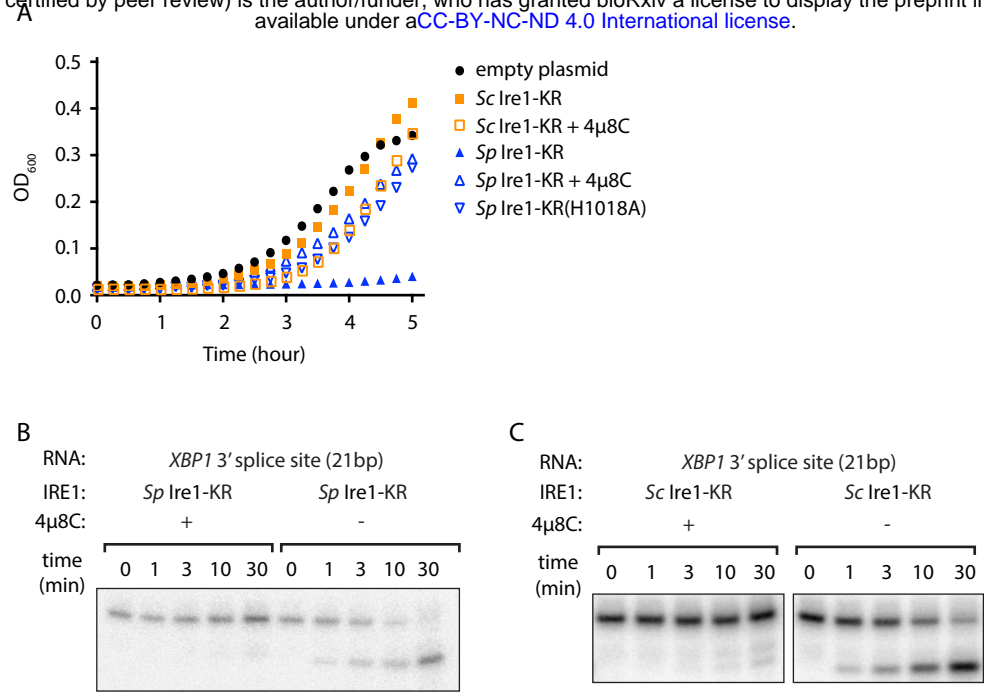
Wang, J., Wang, W., Kollman, P. A., & Case, D. A. (2006). Automatic atom type and bond type perception in molecular mechanical calculations. *J Mol Graph Model*, 25(2), 247-260. doi:10.1016/j.jmgm.2005.12.005

Wang, J., Wolf, R. M., Caldwell, J. W., Kollman, P. A., & Case, D. A. (2004). Development and testing of a general amber force field. *J Comput Chem*, 25(9), 1157-1174. doi:10.1002/jcc.20035

Wiseman, R. L., Zhang, Y., Lee, K. P., Harding, H. P., Haynes, C. M., Price, J., . . . Ron, D. (2010). Flavonol activation defines an unanticipated ligand-binding site in the kinase-RNase domain of IRE1. *Mol Cell*, 38(2), 291-304. doi:10.1016/j.molcel.2010.04.001

Yoshida, H., Matsui, T., Yamamoto, A., Okada, T., & Mori, K. (2001). XBP1 mRNA is induced by ATF6 and spliced by IRE1 in response to ER stress to produce a highly active transcription factor. *Cell*, 107(7), 881-891. doi:10.1016/s0092-8674(01)00611-0

bioRxiv preprint doi: <https://doi.org/10.1101/2021.02.10.430655>; this version posted February 10, 2021. The copyright holder for this preprint (which was not certified by peer review) is the author/funder, who has granted bioRxiv a license to display the preprint in perpetuity. It is made available under aCC-BY-NC-ND 4.0 International license.



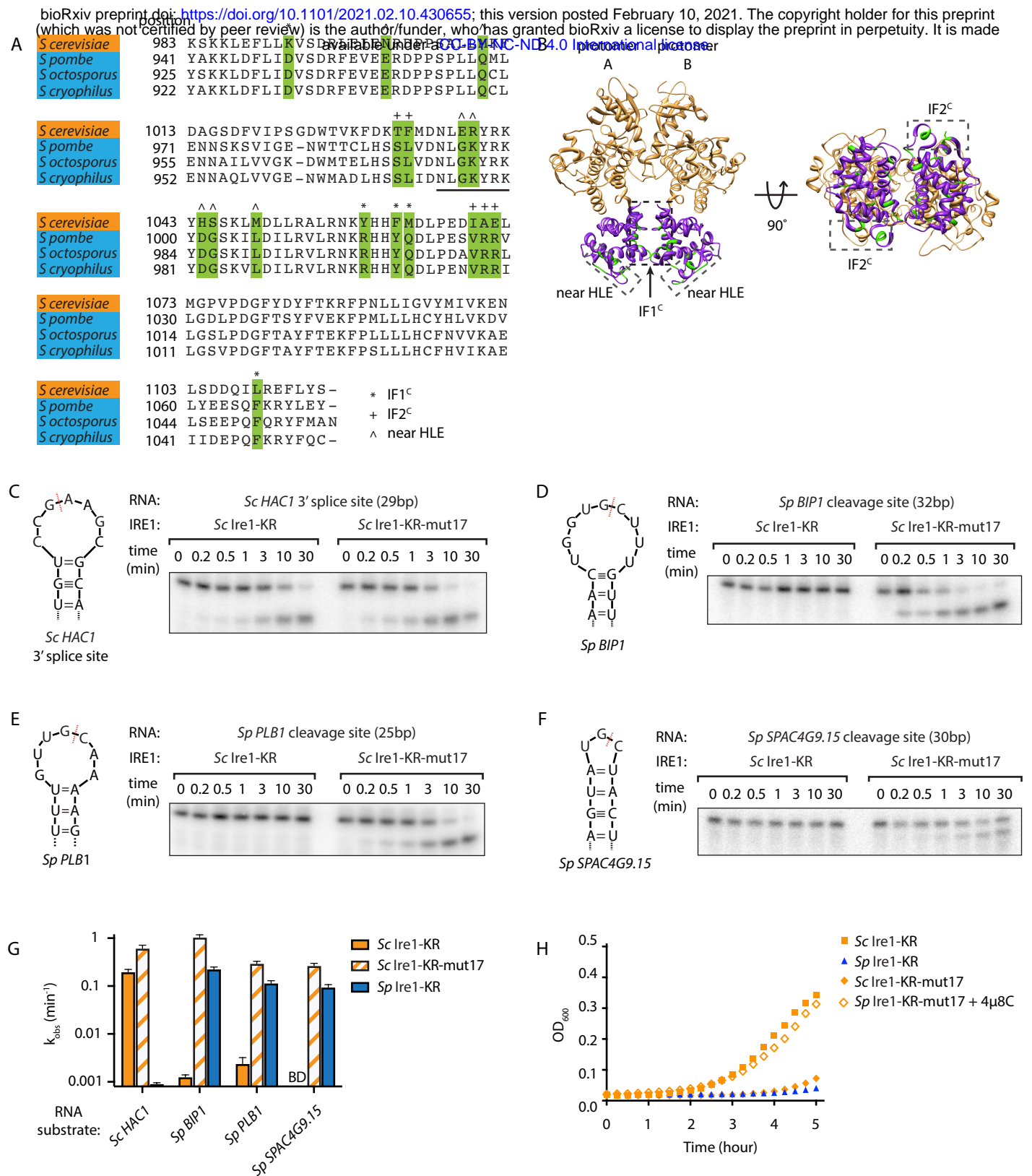


Figure 3 Li & Crotty et al.

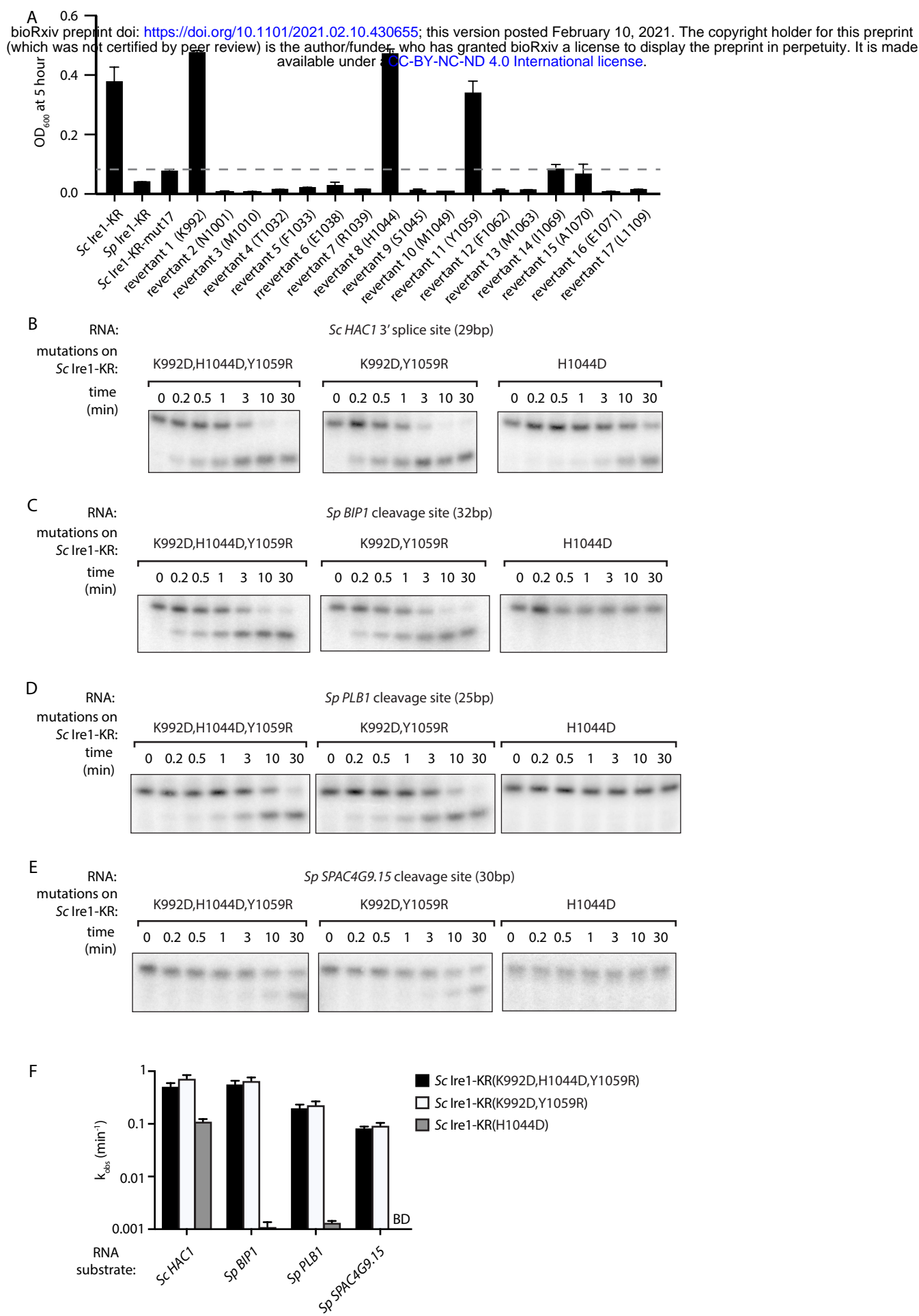


Figure 4. Leong et al.

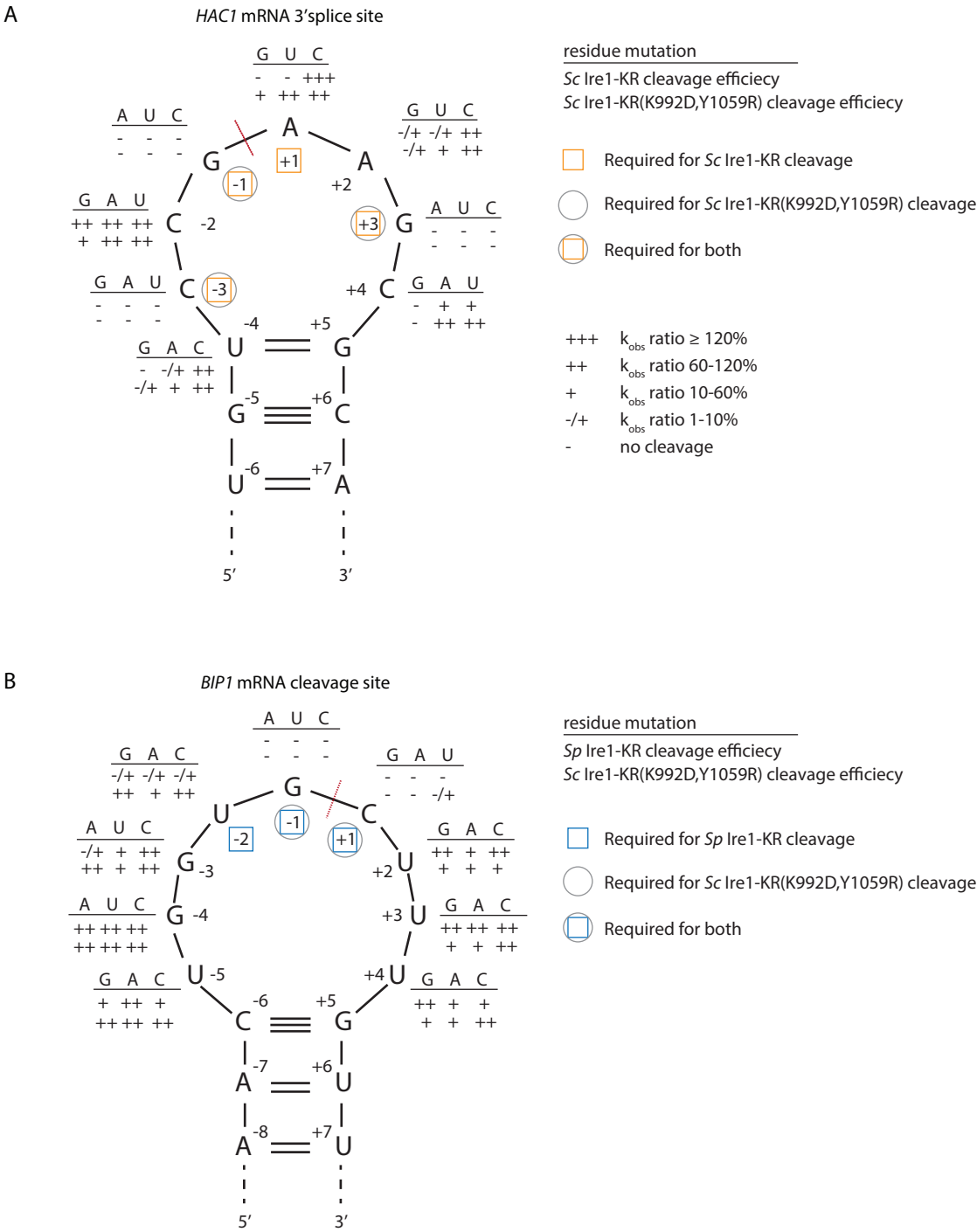
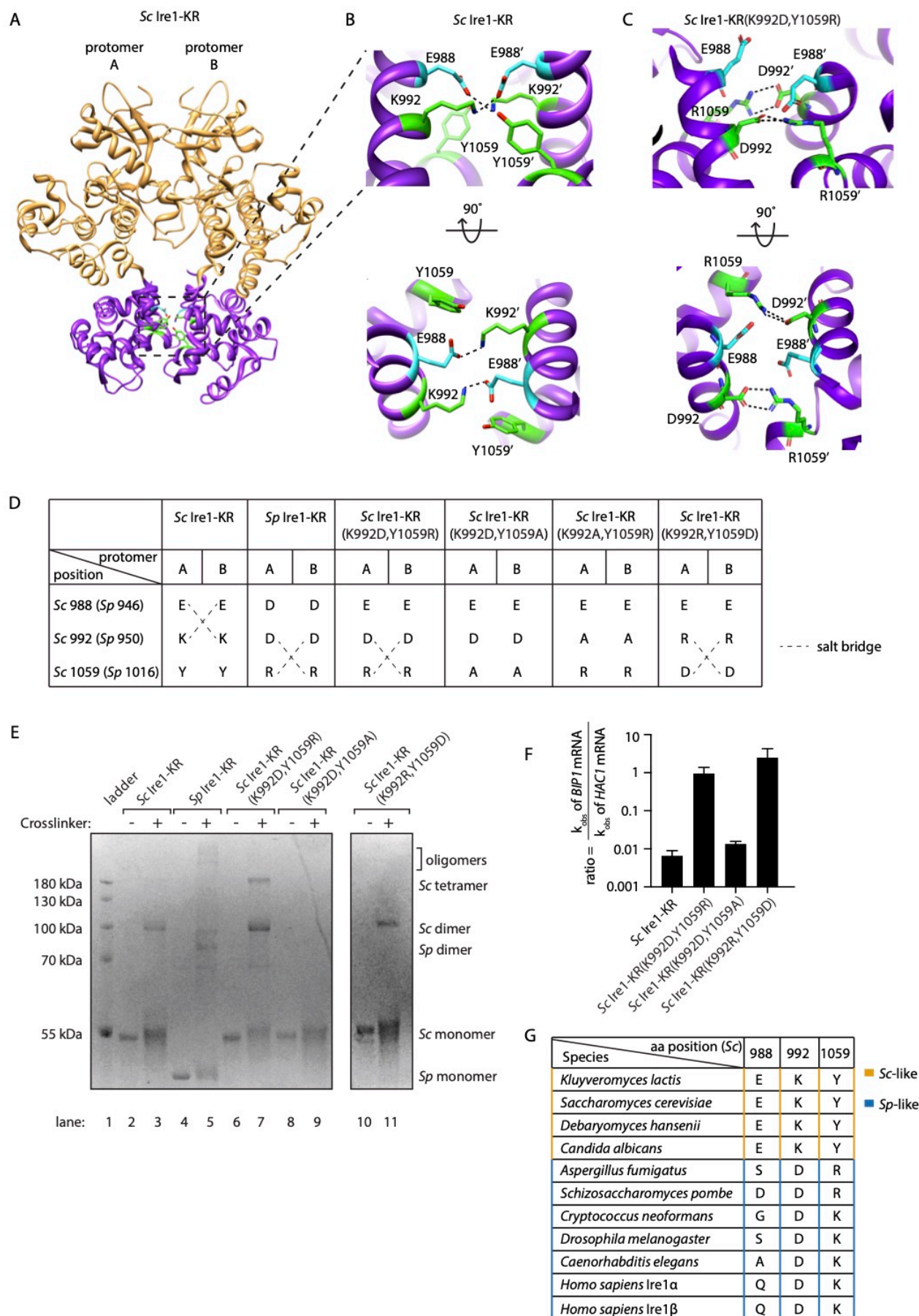


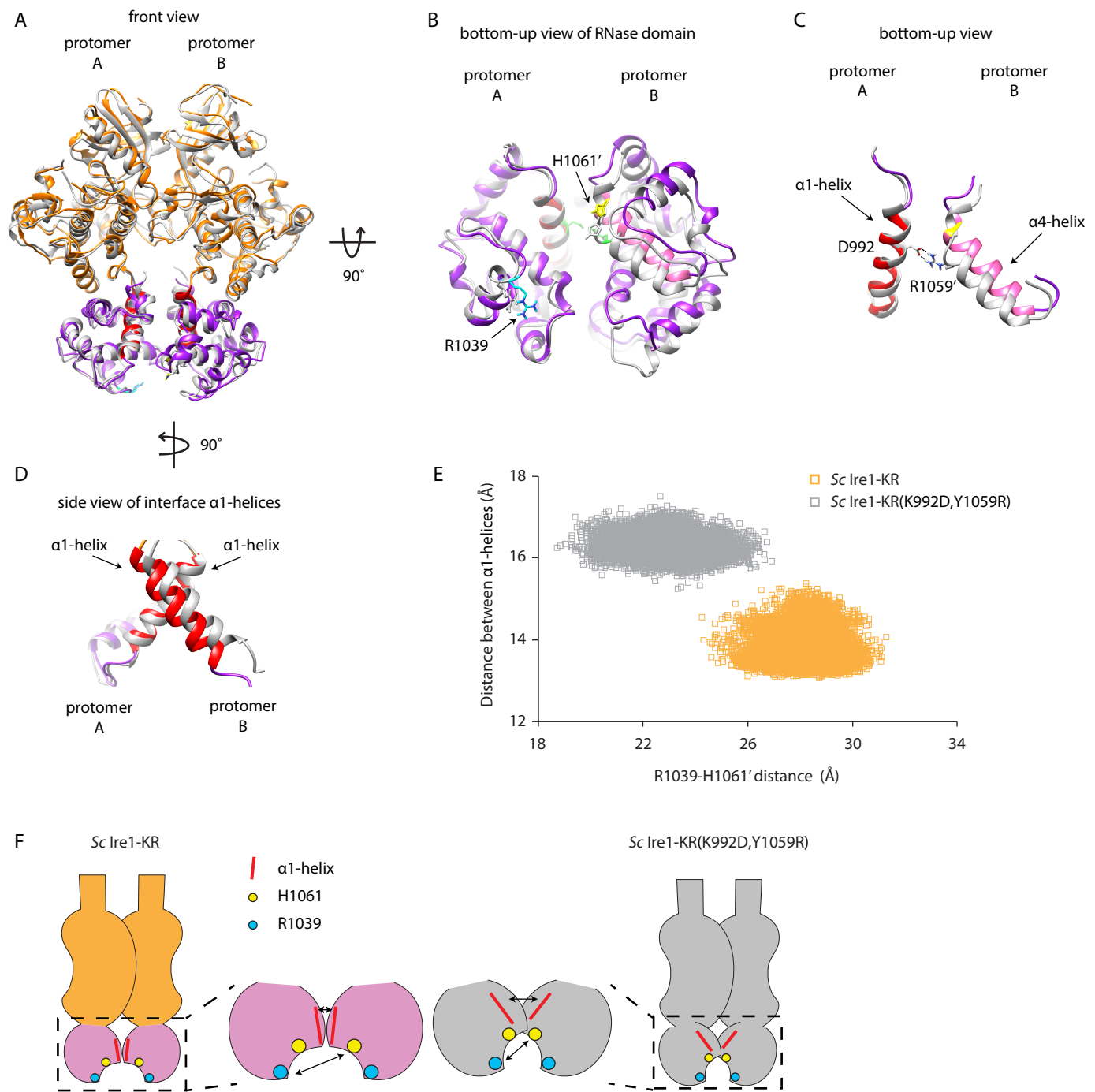


Figure 5

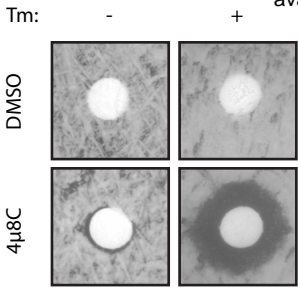




**Figure 6** *Sc Irre1* (which was not certified by peer review) is the author/funder, who has granted bioRxiv a license to display the preprint in perpetuity. It is made available under aCC-BY-NC-ND 4.0 International license.



bioRxiv preprint doi: <https://doi.org/10.1101/2021.02.10.430655>; this version posted February 10, 2021. The copyright holder for this preprint (which was not certified by peer review) is the author/funder, who has granted bioRxiv a license to display the preprint in perpetuity. It is made available under aCC-BY-NC-ND 4.0 International license.



bioRxiv preprint doi: <https://doi.org/10.1101/2021.02.10.430655>; this version posted February 10, 2021. The copyright holder for this preprint (which was not certified by peer review) is the author/funder, who has granted bioRxiv a license to display the preprint in perpetuity. It is made available under aCC-BY-NC-ND 4.0 International license.

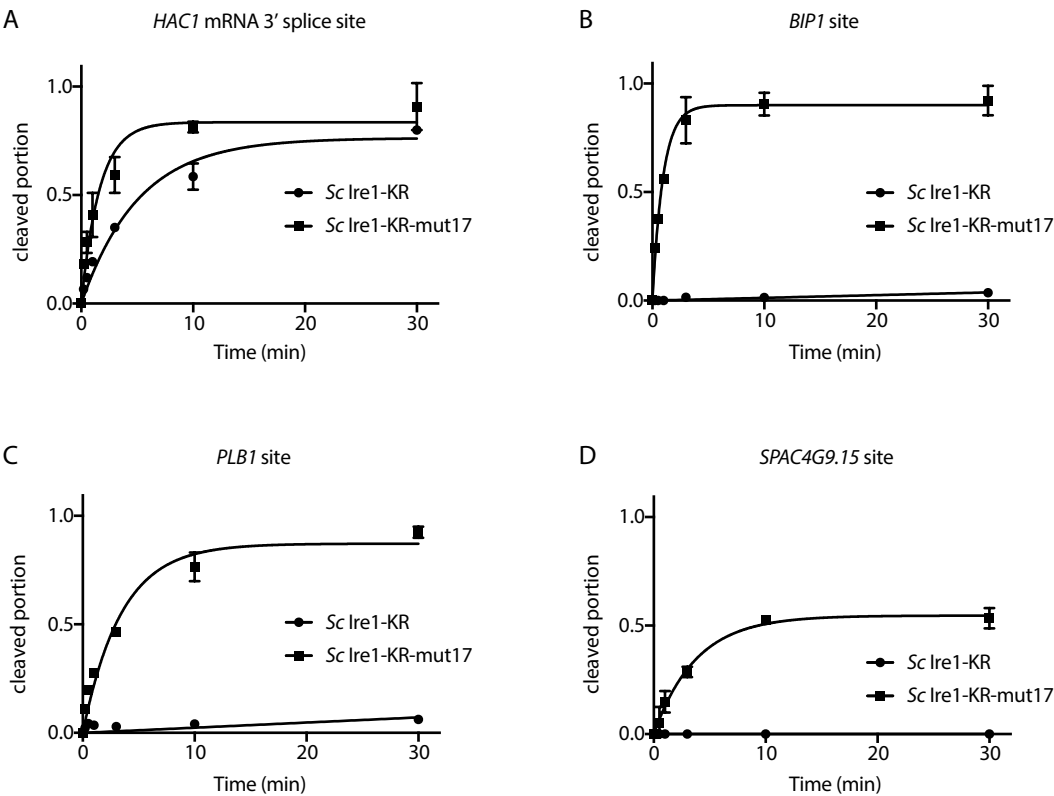
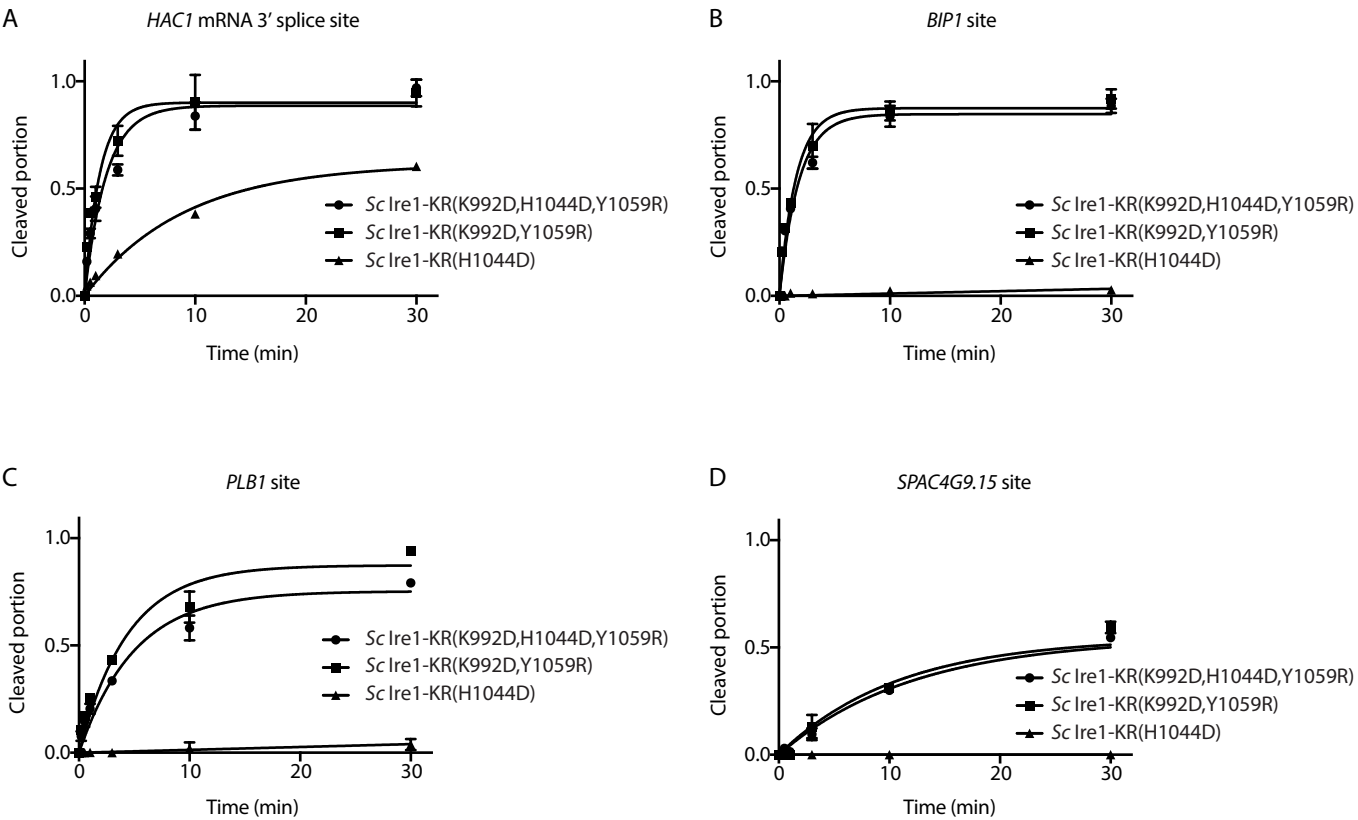


Figure 2 table supplement 1

Lin & Crotty et al.

<i>Sc</i> residue	aa position on <i>Sc</i>	<i>Sp</i> residue	aa position on <i>Sp</i>	location
K	992	D	950	IF1 <sup>C</sup>
N	1001	E	959	HLE
M	1010	Q	968	HLE
T	1032	S	989	IF2 <sup>C</sup>
F	1033	L	990	IF2 <sup>C</sup>
E	1038	G	995	HLE (on HLE)
R	1039	K	996	HLE (on HLE)
H	1044	D	1001	HLE
S	1045	G	1002	HLE
M	1049	L	1006	HLE
Y	1059	R	1016	IF1 <sup>C</sup>
F	1062	Y	1019	IF1 <sup>C</sup>
M	1063	Q	1020	IF1 <sup>C</sup>
I	1069	V	1026	IF2 <sup>C</sup>
A	1070	R	1027	IF2 <sup>C</sup>
E	1071	R	1028	IF2 <sup>C</sup>
L	1109	F	1066	IF1 <sup>C</sup>

bioRxiv preprint doi: <https://doi.org/10.1101/2021.02.10.430655>; this version posted February 10, 2021. The copyright holder for this preprint (which was not certified by peer review) is the author/funder, who has granted bioRxiv a license to display the preprint in perpetuity. It is made available under aCC-BY-NC-ND 4.0 International license.



# Figure 3-table supplement 1

La & Clouty et al.

	K992D	N1001E	M1010Q	T1032S	F1033L	E1038G	R1039K	H1044D	S1045G	M1049L	Y1059R	F1062Y	M1063Q	I1069V	A1070R	E1071R	L1109F
Sc Ire1-KR	N	N	N	N	N	N	N	N	N	N	N	N	N	N	N	N	N
Sc Ire1-KR-mut17	Y	Y	Y	Y	Y	Y	Y	Y	Y	Y	Y	Y	Y	Y	Y	Y	Y
revertant 1	N	Y	Y	Y	Y	Y	Y	Y	Y	Y	Y	Y	Y	Y	Y	Y	Y
revertant 2	Y	N	Y	Y	Y	Y	Y	Y	Y	Y	Y	Y	Y	Y	Y	Y	Y
revertant 3	Y	Y	N	Y	Y	Y	Y	Y	Y	Y	Y	Y	Y	Y	Y	Y	Y
revertant 4	Y	Y	Y	N	Y	Y	Y	Y	Y	Y	Y	Y	Y	Y	Y	Y	Y
revertant 5	Y	Y	Y	Y	N	Y	Y	Y	Y	Y	Y	Y	Y	Y	Y	Y	Y
revertant 6	Y	Y	Y	Y	Y	N	Y	Y	Y	Y	Y	Y	Y	Y	Y	Y	Y
revertant 7	Y	Y	Y	Y	Y	Y	N	Y	Y	Y	Y	Y	Y	Y	Y	Y	Y
revertant 8	Y	Y	Y	Y	Y	Y	Y	N	Y	Y	Y	Y	Y	Y	Y	Y	Y
revertant 9	Y	Y	Y	Y	Y	Y	Y	Y	N	Y	Y	Y	Y	Y	Y	Y	Y
revertant 10	Y	Y	Y	Y	Y	Y	Y	Y	Y	N	Y	Y	Y	Y	Y	Y	Y
revertant 11	Y	Y	Y	Y	Y	Y	Y	Y	Y	Y	N	Y	Y	Y	Y	Y	Y
revertant 12	Y	Y	Y	Y	Y	Y	Y	Y	Y	Y	Y	N	Y	Y	Y	Y	Y
revertant 13	Y	Y	Y	Y	Y	Y	Y	Y	Y	Y	Y	Y	N	Y	Y	Y	Y
revertant 14	Y	Y	Y	Y	Y	Y	Y	Y	Y	Y	Y	Y	Y	N	Y	Y	Y
revertant 15	Y	Y	Y	Y	Y	Y	Y	Y	Y	Y	Y	Y	Y	Y	N	Y	Y
revertant 16	Y	Y	Y	Y	Y	Y	Y	Y	Y	Y	Y	Y	Y	Y	Y	N	Y
revertant 17	Y	Y	Y	Y	Y	Y	Y	Y	Y	Y	Y	Y	Y	Y	Y	Y	N
Sc Ire1-KR(K992D,H1044D,Y1059R)	Y	N	N	N	N	N	N	Y	N	N	Y	N	N	N	N	N	N
Sc Ire1-KR(K992D,Y1059R)	Y	N	N	N	N	N	N	N	N	N	Y	N	N	N	N	N	N
Sc Ire1-KR(H1044D)	N	N	N	N	N	N	N	Y	N	N	N	N	N	N	N	N	N

"N": the mutation is absent in the Ire1 construct  
 "Y": the mutation is present in the Ire1 construct

## Figure 5-figure supplement 1

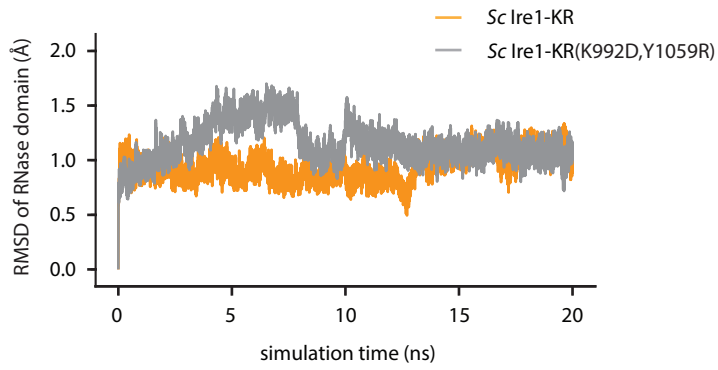
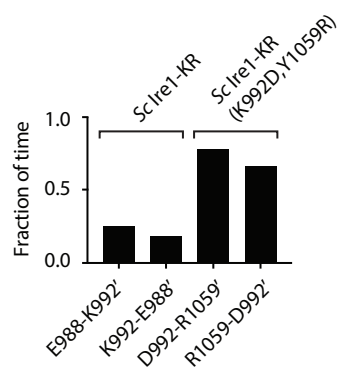
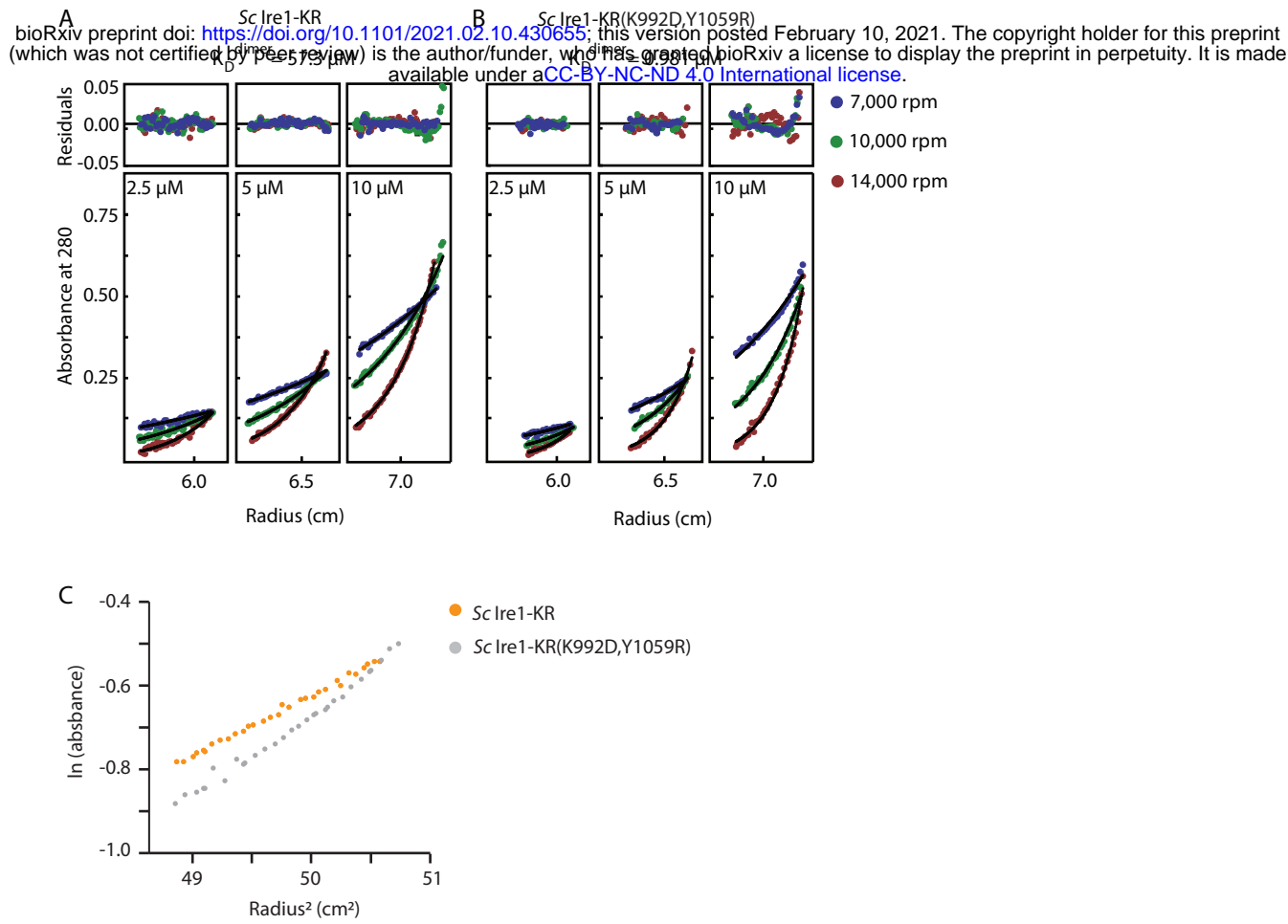


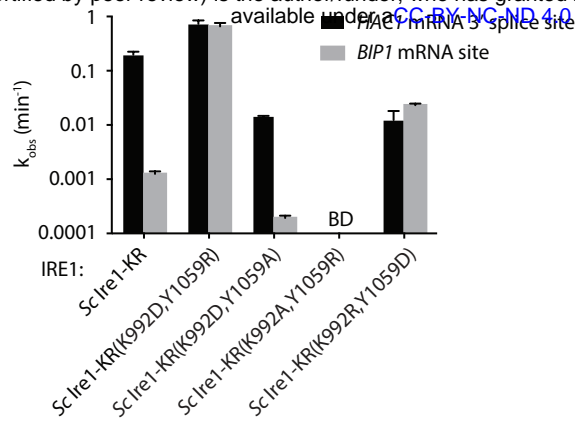
Figure 5-figure supplement 2







bioRxiv preprint doi: <https://doi.org/10.1101/2021.02.10.430655>; this version posted February 10, 2021. The copyright holder for this preprint (which was not certified by peer review) is the author/funder, who has granted bioRxiv a license to display the preprint in perpetuity. It is made available under aCC-BY-NC-ND 4.0 International license.



bioRxiv preprint doi: <https://doi.org/10.1101/2021.02.10.430655>; this version posted February 10, 2021. The copyright holder for this preprint (which was not certified by peer review) is the author/funder, who has granted bioRxiv a license to display the preprint in perpetuity. It is made available under aCC-BY-NC-ND 4.0 International license.

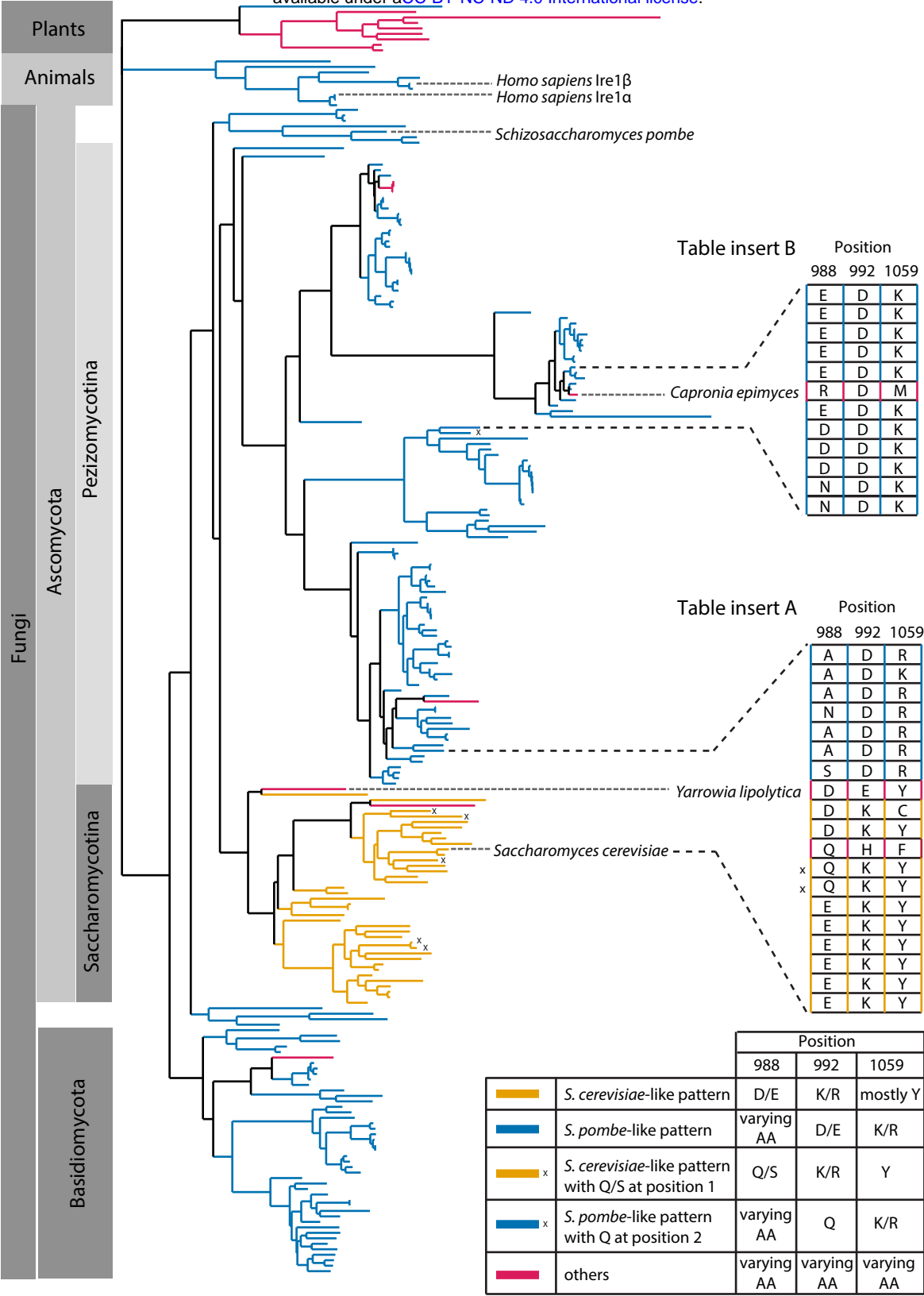


Table 1 LRP & Crotty et al.

plasmid number	description	source
pPW1477	<i>Sc</i> Ire1-KR on pGEX6P-2	Korennnykh et al., 2009
pPW3205	<i>Sp</i> Ire1-KR on pGEX6P-2	Li et al., 2018
pPW3244	<i>Sc</i> Ire1-KR-mut17 on pGEX6P-2	This study
pPW3262	<i>Sc</i> Ire1-KR(K992D,Y1059R) on pGEX6P-2	This study
pPW3263	<i>Sc</i> Ire1-KR(K992D,H1044D,Y1059R) on pGEX6P-2	This study
pPW3256	revertant 1 (K992) on pGEX6P-2	This study
pPW3245	revertant 2 (N1001) on pGEX6P-2	This study
pPW3246	revertant 3 (M1010) on pGEX6P-2	This study
pPW3247	revertant 4 (T1032) on pGEX6P-2	This study
pPW3248	revertant 5 (F1033) on pGEX6P-2	This study
pPW3257	revertant 6 (E1038) on pGEX6P-2	This study
pPW3258	revertant 7 (R1039) on pGEX6P-2	This study
pPW3259	revertant 8 (H1044) on pGEX6P-2	This study
pPW3260	revertant 9 (S1045) on pGEX6P-2	This study
pPW3249	revertant 10 (M1049) on pGEX6P-2	This study
pPW3250	revertant 11 (Y1059) on pGEX6P-2	This study
pPW3261	revertant 12 (F1062) on pGEX6P-2	This study
pPW3251	revertant 13 (M1063) on pGEX6P-2	This study
pPW3252	revertant 14 (I1069) on pGEX6P-2	This study
pPW3253	revertant 15 (A1070) on pGEX6P-2	This study
pPW3254	revertant 16 (E1071) on pGEX6P-2	This study
pPW3255	revertant 17 (L1109) on pGEX6P-2	This study
pPW3441	<i>Sc</i> Ire1-KR(K992D,Y1059A) on pGEX6P-2	This study
pPW3442	<i>Sc</i> Ire1-KR(K992A,Y1059R) on pGEX6P-2	This study
pPW3443	<i>Sc</i> Ire1-KR(K992R,Y1059D) on pGEX6P-2	This study
pPW3275	<i>Sc</i> Ire1-KR(H1018A) on pGEX6P-2	This study